9-18-2023

A Study on the Impact of Nonlinear Effects on Hyperspectral Sub-Pixel Target Detection

Colin J. Maloney
cm6973@rit.edu

A Study on the Impact of Nonlinear Effects on Hyperspectral Sub-Pixel Target Detection

by

Colin J. Maloney

B.S. Physics, United States Air Force Academy

A thesis submitted in partial fulfillment of the
requirements for the degree of Master of Science
in the Chester F. Carlson Center for Imaging Science
Rochester Institute of Technology

September 18, 2023

Signature of the Author _____

Accepted by _____
Coordinator, M.S. Degree Program Date

CHESTER F. CARLSON CENTER FOR IMAGING SCIENCE
ROCHESTER INSTITUTE OF TECHNOLOGY
ROCHESTER, NEW YORK

CERTIFICATE OF APPROVAL

M.S. DEGREE THESIS

The M.S. Degree Thesis of Colin J. Maloney
has been examined and approved by the
thesis committee as satisfactory for the
thesis required for the
M.S. degree in Imaging Science

Dr. John Kerekes, Thesis Advisor

Dr. Emmett Ientilucci

Dr. Jan van Aardt

Date

A Study on the Impact of Nonlinear Effects on Hyperspectral Sub-Pixel Target Detection

Colin J. Maloney, M.S.
Rochester Institute of Technology, 2023

Supervisor: John Kerekes

Abstract

In the realm of hyperspectral (HS) sub-pixel target detection, the Linear Mixing Model (LMM) proposes that the macroscopic interaction between incident light and materials in a scene may be modeled as linear. For individual pixels in hyperspectral data which contain multiple materials, this means that they may be accurately represented by a linear combination of the spectra of those pure materials, which are often called endmembers. However, when nonlinear mixing, such as shadowing and adjacent reflections, are present, the foundational assumptions of the LMM are violated and its accuracy in predicting target detection performance is reduced. This thesis aims to investigate the impact of such nonlinear effects on the performance of the LMM with regards to a HS sub-pixel target detection task.

To quantify the impact of nonlinear effects, an experimental data collect was completed in September 2022 with a Headwall Nano HSI sensor at RIT's Tait Preserve. The Headwall Nano has 272 bands in the visible to the near-infrared (VNIR) region of the electromagnetic spectrum. This data collect utilized five novel sub-pixel targets designed by Chase Cañas with predetermined fill fractions of 100%, 80%, 60%, 40%, and 20%. In addition to the collection of experimental data, two types of modeling software were leveraged to produce results that were based on the LMM and that utilized a

path-tracing technique which is better able to deal with nonlinear effects.

The Forecasting and Analysis of Spectroradiometric System Performance (FASSP) model was designed to predict HS sub-pixel target detection performance. The LMM is foundational to FASSP's systems' performance computations and is used by FASSP to model the propagation of spectral radiance from a user-specified scene through a MODTRAN-informed atmosphere to a user-defined sensor. FASSP relies on a vast array of user inputs to specify the sensor parameters and post-processing algorithms used to detect a target spectrum. FASSP also includes parameters that can account for the shadowing of the target class. As FASSP has been validated in previous studies, it is a reliable reference that can be used to simulate the performance of the LMM both when nonlinear effects are and aren't present.

The Digital Imaging and Remote Sensing Image Generation (DIRSIG) model was first developed in the 1990s by the Digital Imaging and Remote Sensing (DIRS) lab at the Chester F. Carlson Center for Imaging Science (CIS) at the Rochester Institute of Technology (RIT). DIRSIG utilizes a path-tracing model and the three-dimensional geometry of a scene and the spectral properties of the materials within to generate radiometrically-accurate synthetic data that is able to capture nonlinear effects. As a result of the differences in their modeling paradigms, FASSP and DIRSIG provide two different perspectives on a systems' performance analysis of a HS sub-pixel target detection task.

Four setups were designed for the experimental collect to investigate the

effects of shadowing and non-linear mixing on the performance of the LMM. These four setups were replicated within FASSP and DIRSIG. Five targets with varying fill fraction percentages were painted a distinct color and served as the target class within the scene. To replicate the effects of shadowing, five panels were constructed and placed to shadow the five targets. To induce multiple reflections and spectral contamination, five treeshine reflector (TR) panels were constructed and painted with a bright red paint. To determine the effectiveness of this contamination and to inform specular material descriptions in DIRSIG, the Bi-Directional Reflectance Factor (BRF) of the TR panels was also measured with RIT's Goniometer at the Rochester Institute of Technology version Two (GRIT-T) instrument.

The four setups consisted of a base setup with no shadowing or TR panels, a shadowing panel setup, a TR-S panel setup with both the shadowing and TR panels, and a TR panel setup. Results were produced in the form of predicted mean target radiances, Signal-to-Noise-Ratios (SNRs) and target detection performances in the form of Receiver-Operating Characteristic (ROC) curves, and Area-Under-the-Curves (AUCs).

By leveraging the three sources of data (experimental, the LMM-based FASSP, and the path-tracing DIRSIG), a unique parallel analysis was performed to determine the ability of each modeling approach to deal with shadowing and adjacent reflections. It was found that FASSP's ability to accurately predict mean target radiances, SNRs, and target detection performances was

degraded dramatically relative to DIRSIG when shadowing was present. Its accuracy was also degraded when adjacent reflections were present, but not to the same degree.

Results were also produced to examine the impact of including a description of the TR panel specularity in the DIRSIG simulations; it was found that utilizing a Lambertian TR panel resulted in higher mean target radiances than a specular one, but only when the shadowing was also present. The results from DIRSIG indicated a high level of accuracy, however, more work could be conducted to improve the user inputs to ensure optimal settings.

Acknowledgments

It should not be a particularly surprising statement to note that the work present in this thesis is not just the fruits of my own efforts: numerous people have contributed both directly and indirectly to what you see here.

My advisor, Dr. John Kerekes, has been a steady, persistent force in my life for the past two years. He has kept me on track, fielded hundreds of questions, and provided guidance and mentorship that many other students would probably envy. My committee members, Dr. Jan van Aardt and Dr. Emmett Ientilucci, have also kept me on track. These people are also just some phenomenal human beings who make you so happy to be alive when you are in their presence.

As is often the case with family, my parents and siblings have been there for me from the beginning, often kicking my butt when I appeared to not be working and providing something that only family can provide. My mom and dad, in particular, have kept me sane with the insanity of buying a dilapidated house and with becoming an adult. My love and appreciation for them knows no bounds. My friends, both local and remote, have been a special light in my life for these last two years. If I were to measure the quality of my life by the quality of those whom I am fortunate enough to call my friends, I would be the richest man alive.

Table of Contents

List of Tables

List of Figures

Chapter 1

Introduction

Since the development of the Airborne Imaging Spectrometer (AIS) in the early 1980s, remote Hyperspectral Imaging (HSI) sensors have flown above the Earth and collected high resolution spectral and spatial information about its surface and atmosphere [10]. These passive optical sensors collect photons from narrow spectral bands in both the reflective and emissive parts of the electromagnetic spectrum and use that data to create three-dimensional hypercubes with spatial width, x, spatial height, y, and spectral depth, λ.

The design of HSI sensors has undergone many improvements over the years, but despite these iterative steps forward, there exist many complications that still make the accurate collection of Hyperspectral (HS) information difficult. The rest of this introduction will provide some of the basics of HSI (Section 1.1), some relevant previous work which this thesis builds upon (Section 1.2), and the objectives and hypothesis of this work (Section 1.3).

1.1 Fundamentals of Remote Hyperspectral Imaging

Any object that is warmer than absolute zero emits some form of energy, some of which is in the form of Electromagnetic (EM) radiation. Most types of passive Electric-Optical and Infrared (EO/IR) sensors collect EM radiation that has been emitted by either the Sun or by the Earth itself. Radiation which is captured by these sensors is converted to an electrical signal and then quantized into a Digital Count (DC) through the electrical systems of the sensor. This conversion process from EM radiation (photons) to electrons is not 100% efficient, and as a result, characterization of this process is important in order to properly calibrate a sensor. As a part of this conversion process, all EO/IR sensors possess a Relative Spectral Response (RSR) which characterizes their sensitivity to various wavelengths of light.

The amount of photons emitted for a given wavelength can be theoretically determined by Planck's Blackbody Equation, which itself is a function of temperature and wavelength [8]. For the sun, which has a temperature of approximately 5800 K, the peak of its blackbody curve resides within the visible portion of the electromagnetic spectrum, around 500 nanometers (nm). For the Earth, which has a temperature around 290 K, most of the photons are emitted in the Midwave Infrared (MWIR) and Longwave Infrared (LWIR) regions of the EM spectrum [8]. Passive optical sensors collect these emitted photons and are often designed so that they only capture those photons in certain regions of the spectrum. Many of these restrictions in wavelength-

dependent sensitivity is due as well to the type of photodiode which is used - for example, silicon photodiodes generally have optimal sensitivity to photons with wavelengths in the visible region of the EM spectrum but lose sensitivity in the Ultraviolet (UV) and Near-infrared (NIR) regions of the spectrum [25].

Most commercial cameras (such as the one on a cell phone) possess three spectral bands (red, green, and blue), which are sensitive to EM radiation at many wavelengths in the visible part of the spectrum. These sensors attempt to mimic the RSRs of the cones in the average human eye [8]. However, because the individual bands in an RGB sensor are sensitive to many different wavelengths of light, these sensors are not generally signal-starved in 'well-illuminated' scenes. As a result, over time, the spatial dimensions of the individual pixels in these sensors have been reduced and the quantity of pixels has been increased. This improves the spatial resolution of a sensor which allows for finer resolution of the spatial irregularities of a scene. However, because these sensors only have three bands, a given pixel in an RGB sensor captures very little spectral information about the incident EM radiation.

Hyperspectral imaging (HSI) sensors are often designed with the aim of increasing the number of spectral bands within a sensor without significantly reducing the spatial resolution. This is a challenge - when spectral bands are narrower, it is easier for individual pixels in HSI sensors to become 'signal-starved'. To address this, the physical dimensions of the individual pixels within an HSI sensor are made larger, which in turn reduces the spatial reso-

lution [8]. As a result of this reduction of spatial resolution, it becomes more difficult (if not impossible) to resolve objects that are physically smaller than the size of one projected pixel. This is the defining motivation for research into the realm of sub-pixel target detection; detecting sub-pixel targets with HSI sensors often relies on leveraging the additional spectral information within a pixel, rather than attempting to spatially resolve a target.

The situation is made more complex when dealing with remote sensors - that is, those sensors that are physically distant from the scene which is to be imaged. Despite the challenges, the ability to remotely collect HSI data with high spectral and spatial resolution carries with it many applications. HSI sensors have been used for a myriad of applications, including geological analysis and mineral mapping [39], and target detection [27]. The collection of HSI data may be best described as an 'imaging chain', which may broken down into several parts: material spectroscopy, radiative transfer, imaging spectrometry, and data processing [8]. These components of the imaging chain will be discussed in more detail in Chapter 2.

There exists at least two theoretical models that attempt to describe the structure of HSI data: the Linear Mixing Model (LMM) and the Stochastic Mixture Model (SMM) [8]. Both of these models endeavor to accurately describe what the interaction of light with materials in a scene looks like to an HSI sensor. The focus of this thesis is on the LMM, which proposes that, on a macroscopic scale of meters, the interaction of incident photons with a

material may be modeled as essentially linear. This means that the HSI data that is recorded for a given pixel may be represented as a linear combination of all present pure materials' spectra weighted by the proportion of the area that these materials occupy within the ground-projected area of that pixel. These pure materials are often called *endmembers*. The accuracy of the LMM is dependent on the validity of some vital assumptions: that the sensor response is linear, that illumination conditions within a projected pixel are uniform, and that there exists no nonlinear interactions between the incident light (such as the light reflected off of one surface before striking another) [8].

As mentioned above, to support the work of this thesis, two types of modeling software have been used to generate results for our analysis. The Forecasting and Analysis of Spectroradiometric System Performance (FASSP) model [23, 24, 42] utilizes the LMM to perform system requirement analyses with respect to sub-pixel target detection tasks. The most important results from FASSP that are used for comparison are target radiances and Receiver Operating Characteristic (ROC) curves. ROC curves depict the ability of a sensor (and the accompanying data processing) to distinguish between target pixels (successful detections) and non-target pixels (false alarms). As it is based on the LMM and has been validated by various tasks, FASSP serves as an accurate assessment of LMM performance.

The other type of modeling software used in this thesis is the Digital Imaging and Remote Sensing Image Generation (DIRSIG) model, which

was developed and is maintained by RIT's Digital Imaging and Remote Sensing (DIRS) Lab. DIRSIG has been validated in numerous publications as its functionalities have been expanded and improved upon since the early 1990s [11, 28, 33]. DIRSIG utilizes a three-dimensional rendering of a scene with spectral and specular descriptions of the materials within that scene to generate radiometrically-accurate synthetic data. To calculate how this scene 'looks' to a sensor, DIRISG utilizes a path-tracing model which propagates EM radiation to generate synthetic data for a wide variety of remote sensing platforms. As it is not based on the LMM, DIRSIG offers an alternative perspective from which it is possible to analyze how the LMM breaks down when its fundamental assumptions are violated. More background on FASSP and DIRSIG will be given in Chapter 2.

1.2 Previous Work

There exists a wealth of previous work upon which this thesis aims to build on. This work can be best broken down into three main types: the theoretical modeling of HSI data, the development of modeling software for system analysis and the collection of experimental data with setups that incur nonlinear impacts on the target spectra.

In their 2012 paper, Bioucas-Dias et. al. examined the multitude of mixing models which have been used to assist with the problem of spectral unmixing in HSI data [2]. In their paper, they note the nuances associated with

defining the endmembers and their associated abundances within a given pixel; one particularly interesting observation they make is that when examining the spectra of a specific pixel, the spectrum of a small, but reflectively-bright object can dominate that of a larger, but less-bright object. They state that Linear Mixing (LM) holds when the scale of mixing is 'macroscopic', that is when the minimum dimensions of the individual materials are larger than a few centimeters, as was noted in the 1979 paper from Dr. Robert Singer and Dr. Thomas McCord when they examined the mixing of spectra of dark and bright materials on the surface of Mars [37].

Bioucas-Dias et. al. also observe that when nonlinear mixing occurs due the scattering of light by multiple materials in a scene, it can viewed as occurring on one of two levels: the classical/multilayered level and the microscopic level. The classical level examines light on the macroscopic scale; the multilayered model views these multiple reflections as an infinite sequence in which the first term is often sufficient for most applications. The microscopic level views nonlinear mixing as occurring when photons are emitted from molecules of one material and absorbed by the those of another material, and in turn, emitted again: the apparent albedo of a mixture of materials is viewed as the mixture of a linear average of the albedos of the constituent materials. The work presented in this thesis uses the classical level view of nonlinear mixing.

In 2012, to improve the identification of endmember abundances in

HSI data, Somers et. al. published their work on the development of a new endmember extraction algorithm (EEA), which by reducing the variability of endmember spectra, yielded improved abundance estimations [38]. They note that currently available automated EEAs fail to deal properly with the natural variation that exists within and between endmember spectra, and so by utilizing subsets of the data to better define in-scene variability of endmember spectra, they can use reduction techniques to improve endmember abundance estimates.

This thesis aims to build upon the wealth of research behind the LMM and spectral unmixing by conducting a data collect which in which controlled nonlinear effects will be imposed. These nonlinear effects will allow us to examine the independent effects that shadowing and multiple reflections have on a spectral unmixing task, by attempting to determine whether a known target endmember exists within a pixel. This research will also be examined in the data analysis of our FASSP and DIRSIG results. In contrast to [38], this work does not aim to necessarily improve the identification of endmember abundances, but to instead understand the impact that various nonlinear effects have on the ability of a system to determine whether an endmember is present in a pixel.

As mentioned above, the two types of modeling software that are relevant to this thesis are FASSP and DIRSIG. FASSP was developed first in the early 2000s by Dr. John Kerekes and Jerrold Baum to predict system perfor-

mance analysis in the solar reflective portion of the EM spectrum (0.4 microns to 2.5 microns) [23]; it was initially validated when it accurately predicted target radiances, sensor SNRs, and detection performance that matched up with experimental data from HYDICE [32]. FASSP was later expanded to operate in the thermal-emissive portions of the EM spectrum (2.5 microns out to 14 microns) [24] and was validated with LWIR HSI data collected by SEBASS [13].

DIRSIG was initially developed in 1990s by the DIRS lab at RIT and it is currently available in its fifth iteration (DIRSIG5) [11]. The first version of DIRSIG3 to be publicly-distributed was DIRSIG3 in 2003 [22]. DIRSIG was first validated with MWIR/LWIR imagery of a parking lot at RIT in two separate data collects in 1994 and 1995 [4, 28] and later with VIS/NIR/SWIR HSI data from HYDICE [3]. DIRSIG has also been validated with respect to its ability to accurately simulate low-light sources [20], spectral texture variability [34], polarized Bi-directional Reflectance Distribution Functions (BRDFs) [36], and Light Detection and Ranging (LIDAR) [5], as well as others.

This thesis aims to utilize FASSP and DIRSIG to produce results for a subpixel target detection task. These results are produced for when nonlinear effects are and are not present, and as such, should allow for an exploration into FASSP and DIRSIG accuracy relative to the experimental results for when nonlinear effects are and are not present. This analysis allows for an examination of how well a LMM-based model (FASSP) and a path-tracing model

(DIRSIG) deals with the phenomena of shadowing and multiple reflections.

A plethora of work has also been conducted to collect HSI experimental data that is relevant to the work in this thesis. In 2010 and 2012, HSI data was collected in various locations in upstate New York as a part of the SpecTIR Hyperspectral Airborne Rochester Experiment (SHARE) effort [9, 15]. In these collection campaigns, a pair of 3×3 meter and 2×2 meter red and blue felt target panels were placed in nine configurations with varying illumination conditions and backgrounds. The target panels were placed in the open, in full shade, and in partial shade; they were also placed on dirt, gravel, roof tar paper, and grass. Notably, the targets were also placed under and around tree canopies so as to investigate the impact of the spectral contamination from the surrounding vegetation (the so-called 'treeshine effect'). The objective behind this was to examine the impact of varying illumination conditions, background setups, and the adjacency effect on a target detection task.

Follow-on research to the SHARE 2010/2012 collect included an analysis of the impacts of varying the illumination conditions and background type [16]. Ientilucci noted that placing the targets on the gravel versus on the grass resulted in significant differences; this is attributed to the adjacency effect from the grass background. Ientilucci also examined the impact of shadowing on the spectral radiances of the red and blue felt panels and notes a large magnitude difference between those panels placed out in the open and those placed in the shade. With the blue panels, specifically, he noticed that the

target radiances and reflectances are increased in the blue region of the EM spectrum due to the indirect blue scattered light from the atmosphere for those targets in shadow. Finally, Ientilucci took a look at the target detection task and found that unstructured and covariance-based algorithms have the ability to whiten spectra, and as such, are able to locate those target pixels in shadow better with the Adaptive Cosine Estimator (ACE) and the Matched Filter (MF) algorithms than other algorithms.

Subsequent research also included an assessment of the target detection task, when Ientilucci utilized the SHARE 2010/2012 data to determine detection capabilities of the targets in the various illumination conditions and background setups [17]. This analysis was performed on the red and blue felt target panels on grass, gravel, and roof tar paper backgrounds and in fully illuminated and heavy and light shadowed areas. Ientilucci utilized several target detection algorithms including the Spectral Angle Mapper (SAM), the Matched Filter (MF), and the Adaptive Cosine Estimator (ACE). He also generated truth masks using ENVI. In addition to validating the SHARE 2012 data with that from the SHARE 2010, it was determined that the target pixels which were in shadow were more difficult to find than those in the open.

In addition to his other analyses, Ientilluci utilized LIDAR data in conjunction with HSI data to investigate conduct a target detection analysis by using the LIDAR data to obtain pixel-specific solar and sky-loading scaling factors to better estimate the spectra of shadowed targets in the HSI data

[18]. In his 2012 paper, Ientilucci investigated the impact of reducing and eliminating direct solar illumination has on a target's spectral radiance. He also discussed the target spectral contamination that occurs as a result of nearby objects/materials. By leveraging the LIDAR point cloud data to generate per-pixel to estimate estimates of the viewable sky and the direct solar illumination, Ientilucci was able to improve target detection capabilities of a shadowed blue felt panel.

In addition to examining the SHARE 2010/2012 data, Ientilucci and Gartley have also examined the impact of specular behavior (BRDF) on target detection and found that the spectral character of different materials tended to converge with one another as the specularity of those materials increased; they ultimately concluded that BRDF effects could cause potential false alarms in a target detection task [21].

This work aims to add to the vast repository of HSI data sets that currently exist. The data set produced by this work is different in several ways. It imposed *controlled* nonlinear effects with precisely-constructed and arranged panels. In addition, the targets used by this work's data set were novel sub-pixel targets [7] which were sampled with a high spatial resolution of approximately 4 cm Ground Sample Distance (GSD).

This work aims to build upon prior work with the SHARE 2010/2012 data by further investigating the impact of various illumination conditions on a target detection setup by utilizing panels which are painted bright red and are

intended to contaminate the target panels' spectra. In contrast to Ientilucci's and Gartley's work investigating the impact of a target's specularity on its ability to be detected [21], this thesis aims to investigate the impact of an adjacent 'bright' panel which is meant to contaminate the spectra of the target panels. This work also aims to build upon Ientilucci's work attempting to compensate shadowed pixels with LIDAR data [18], by better investigating the impact that this shadowing has on a sub-pixel target.

New target detection algorithms have been developed and tried in order to deal with the effects of shadowing and poor illumination. Wiseman and et. al. presented an enhanced ACE detection algorithm, ACE-shadow, which utilized scene-based atmospheric correction methods to more accurately model the shadowed target spectra [40] and ultimately, obtain improved results for shadowed target pixels. This thesis utilizes the Constrained Energy Minimzation (CEM) algorithm to produce target detection performance statistics.

1.3 Objectives and Hypothesis

This thesis aims to complete the following objectives in order to contribute meaningfully to the existing body of work in this regime and also to fulfill the requirements of this degree program.

1. Produce a hyperspectral dataset with controlled nonlinear effects (shadowing and adjacent reflections) which impact a sub-pixel target detection task

2. Evaluate the accuracy of a LMM-based model (FASSP) and a path-tracing model (DIRSIG) at predicting target radiances and target detection performance when these nonlinear effects are present

3. Identify limitations of LMM and opportunities to explore further improvements for more accurate modeling of nonlinear effects

Based on the previous work discussed above in Section 1.2, it is logical to hypothesize that both the LMM-based model (FASSP) and the path-tracing model (DIRSIG) will have reduced accuracies when nonlinear effects are present in our data, however, due to its modeling approach and its ability to capture nonlinear effects, it is anticipated that DIRSIG will be able to more closely approximate the experimental results than FASSP will be able to. This is also because the LMM relies on there existing only linear interactions between incident light and the materials within a scene, so altering the scene setup such that there exists nonlinear interactions should, theoretically, result in inaccurate predictions. DIRSIG can also take as an input an object's BRDF, so by including in the DIRSIG simulations a description of relevant objects' specularity, DIRSIG has a better chance of accurately predicting the impact of adjacent reflections on a target object.

The rest of this thesis is organized as follows. Chapter 2 covers much of the context needed to understand the work in the remainder of this thesis. Chapter 3 discusses the methods that were used to conduct an experimental data collect at Rochester Institute of Technology's (RIT) Tait Preserve in

September 2022, as well as the methods used to process the resulting experimental data and data from two types of modeling software: the Forecasting and Analysis of Spectroradiometric System Performance (FASSP) model and the Digital Imaging and Remote Sensing Image Generation (DIRSIG) model. Chapter 4 presents the results and analysis from these data sources. Chapters 5 and 6 summarizes this work and outlines future avenues that may be worthwhile to pursue. Finally, the Appendix includes relevant, supplemental data that is useful to the especially invested reader.

Chapter 2

Background

This Chapter will discuss all of the context required to explain the work conducted to fulfill the Objectives described in Section 1.3. For the sake of clarity, This Chapter will be broken into several sections: Optical Radiation in Remote Sensing Applications (Section 2.1), Hyperspectral Target Detection (Section 2.2), and Modeling Software (Section 2.3). Section 2.1 will discuss the basics of how EM radiation interacts with materials in a scene, radiative transfer, the science of imaging spectrometry, and data models. Section 2.2 will discuss statistical basis of HS target detection and present some relevant target detection algorithms. Finally, Section 2.3 will discuss the basics of DIRSIG and FASSP.

2.1 Optical Radiation in Remote Sensing Applications

As mentioned in Chapter 1, every passive EO/IR system collects electromagnetic (EM) radiation (light). As this radiation travels around, it interacts with matter in its states (gases, solids, and liquids) in the Earth's atmosphere and on its surface. EM radiation is often described with respect to its wavelength, λ. There exists many different regimes within the EM spec-

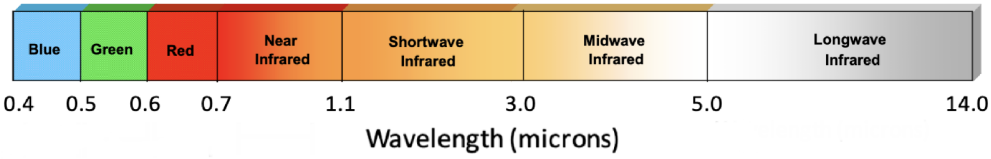

Figure 2.1: The electromagnetic spectrum from 0.4 to 14.0μm. Figure is used courtesy of Eismann [8].

trum that HSI sensors operate in. The first is the VISible (VIS) region, which stretches from 0.4 to 0.7 microns (μm) and represents the extent of the EM spectrum that our eyes can reliably see. Beyond this, there exits the Near-Infrared (NIR, 0.7 to 1.1μm) region, the Shortwave Infrared (SWIR, 1.1 to 3.0μm) region, the Midwave Infrared (MWIR, 3.0 to 5.0μm) region, and the Longwave Infrared (LWIR, 5.0 to 14.0μm) region. Figure 2.1 shows the EM spectrum with the regions described. Incoming EM radiation from the sun dominates in the VIS, the NIR, and the SWIR regions, and as such, this range is referred to as the *solar reflective* region of the spectrum; EM radiation is also emitted by the Earth and dominates in the LWIR region - this range is referred to as the *thermal emissive* region of the spectrum. Due to the unique challenges present in detecting radiation for each of these regions, sensors are often designed to be sensitive in either the reflective or the emissive regions, but not both.

The study of remote HSI can be broken down into 4 basic components: material spectroscopy, radiative transfer, imaging spectrometry, and data models [8]. These parts will be discussed independently in the following

subsections.

2.1.1 Material Spectroscopy

In the most fundamental sense, material spectroscopy seeks to explain how the physical makeup of atoms and molecules impact their resulting interaction with EM radiation. Remote HSI assumes that the features of light that emerge as a result of these interactions may be detected by a remote platform which is physically distant from the location of these interactions. A full understanding of the nature of these interactions is only possible from a quantum mechanics perspective, however, in the realm of HSI, it is helpful to focus on those properties those that can be detected with either lab-based or remote sensors, called the apparent spectral properties. These properties consist of spectral reflectance, absorbance, and transmittance for remote sensors. Of these, reflectance is generally the most important quantity for the purposes of this thesis, which focuses primarily on the solar reflective portion of the EM spectrum.

There exists several ways to describe the spectral reflectance of a material, however this thesis will focus its discussion on the Bidirectional Reflectance Distribution Function (BRDF) and the Directional Hemispherical Reflectance (DHR). As mentioned in the Introduction (Ch. 1), the BRDF is a measure of a material's specularity. To do this, the BRDF relates the incident irradiance, $E(\theta_i, \phi_i, \lambda)$, to the reflected radiance, $L(\theta_r, \phi_r, \lambda)$, of a material. It

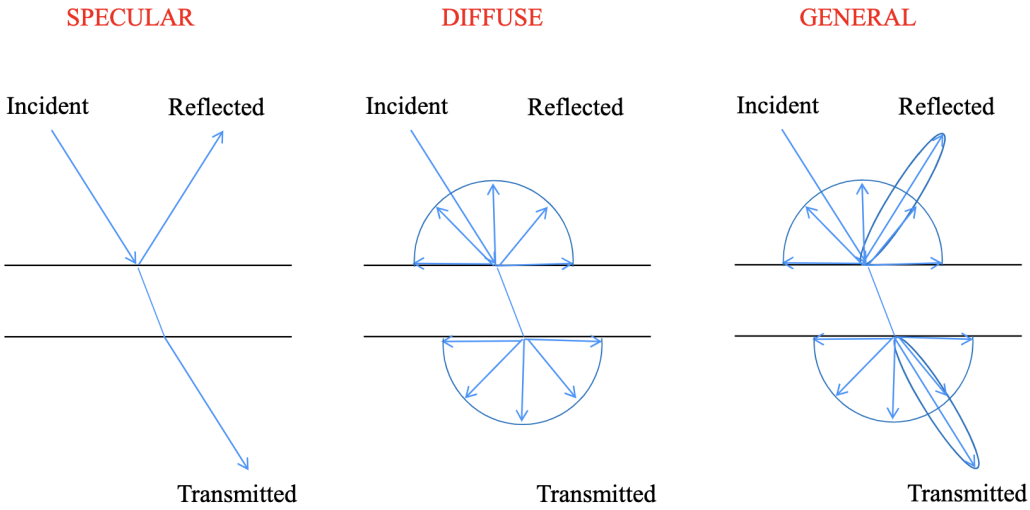

Figure 2.2: Three cases describing three types of materials: a specular material which reflects light in a manner consistent with Snell's Law, a diffuse material which scatters the light uniformly in all directions, and a general (realistic) material, which is a combination of the specular and diffuse materials. Figure is used courtesy of Eismann [8].

has units of sr^{-1} and is dependent on both the incident and reflected angular directionality of the irradiance and radiance. The BRDF is defined in Equation 2.1. A depiction of the BRDF is also shown in Figure 2.2, where three separate types of materials are shown: a specular material, a diffuse material, and a general (realistic) material [8]. In HSI, it is often assumed that a material is Lambertian: that is, that it reflects light equally in every direction, and as such, BRDF effects do not need to be considered.

$$\rho_{BRDF}(\theta_r, \phi_r, \theta_i, \phi_i) = \frac{L(\theta_r, \phi_r, \lambda)}{E(\theta_i, \phi_i, \lambda)} \tag{2.1}$$

The DHR is a measure of the ratio of the total reflected irradiance to the incident irradiance; it is only dependent on the incident angular directionality (θ_i and ϕ_i). Its definition with respect to the BRDF is given in Equation 2.2.

$$\rho_{DHR}(\theta_i, \phi_i, \lambda) = \int_0^{\pi/2} \int_0^{2\pi} \rho_{BRDF}(\theta_r, \phi_r, \theta_i, \phi_i) cos(\theta_r) sin(\theta_r)\, d\phi_r d\theta_r \quad (2.2)$$

It takes a specialized instrument to measure the BRDF of a material. One of these is the Goniometer at the Rochester Institute of Technology version Two (GRIT-T), which was used to measure a closely-related quantity, the Bi-directional Reflectance Factor (BRF) of several materials relevant to this thesis [14]. The BRF is the ratio of the measured radiance of a material to a Spectralon panel with a known radiance [14, 29]. The Spectralon panels are manufactured by Labsphere, Inc. and are designed to be Lambertian; however they are not perfect and measurements are made to account for this post-processing. To make its measurements, GRIT-T uses an ASD FieldSpec4 High Resolution Spectrometer from Malvern Panalytical. To take into consideration the directionality of these measurements, the reflected spectrum is measured at constant intervals over the entire hemisphere above a material.

The spectral DHR is easier to measure and can be done with any Multispectral Imaging (MSI) or HSI sensor. When a material can be reasonably assumed to be Lambertian, the relationship $\rho_{BRDF}(\lambda) = \frac{\rho_{DHR}(\lambda)}{\pi}$ is commonly used to relate the DHR to the BRDF of a material. Figure 2.3 shows the

detected spectral reflectances of various natural materials from the VIS to the SWIR regions of the EM spectrum.

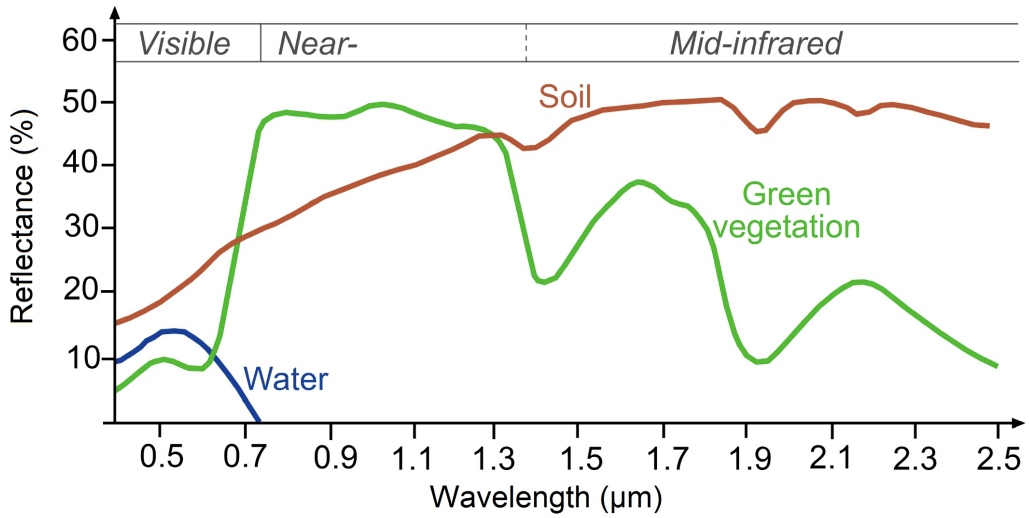

Figure 2.3: The spectra of various natural materials in terms of their relative reflectances. Note the sharp 'red edge' of the green vegetation at $0.7\mu m$. Figure is used courtesy of Ossietzky [35] as a part of the Creative Commons Attribution-Non-Commercial-ShareAlike 2.0 Generic (CC BY-NC-SA 2.0) license.

Each of these materials have a distinct spectrum; these differences come from the unique atomic makeups and physical arrangements that each of these materials possess. The same material can appear quite dissimilar in varying circumstances to an HS sensor: the illumination source, the atmosphere, and BRDF-effects all impact the resulting spectrum. The atmosphere, in particular, is responsible for a large source of variance and noise in HSI. Fortunately, various modeling methods have been developed to better understand and compensate for the atmosphere's effect.

2.1.2 Radiative Transfer

For an airborne or spaceborne HS sensor, EM radiation must invariably travel through some portion of the Earth's atmosphere. During this trip, there exists a chance of it being absorbed or scattered by the various atmospheric gases. These interactions are spectral in their nature as they occur at widely-varying rates for different wavelengths of light.

Atmospheric absorption occurs when a molecule in the atmosphere absorbs incident radiation. Not all of the gases which are prevalent in the atmosphere readily absorb light. For example, nitrogen, which is by far the most abundant gas within the atmosphere, absorbs and scatters relatively small quantities on the incoming radiation, whereas water vapor, carbon dioxide, ozone, and liquid water all have much more significant impacts [8]. Water vapor, in particular, can play a severely detrimental impact on remote sensing capabilities. The location and magnitude of the so-called 'absorption bands' created by these gases is dependent on their respective molecular compositions.

Atmospheric scattering occurs when an incoming photon strikes a molecule in the atmosphere and is deflected from its original course. In general, there are two basic models which describe the amount of scattering as a function of wavelength. Rayleigh scattering accurately describes the amount of scattering in the atmosphere due to small diameter molecules in the atmosphere; it proposes that the amount of scattering is proportional to $\frac{1}{\lambda^4}$, and as a result, scattering due to smaller molecules increases to the power of 4 with shorter

wavelengths [8]. Mie scattering accurately describes the scattering due to larger molecules within the atmosphere, such as smog and smoke. As such, it is often more prevalent over cities and regions with large amounts of human activity [8].

In formal terms, the study of Radiative Transfer (RT) is the study of the way EM radiation interacts with objects within a scene and the atmosphere, which ultimately results in the spectral radiance which is measured at the sensor aperture. There are several mechanisms by which light from a source may interact with objects in a scene. Figure 2.4 shows several of these for the solar reflective part (VIS, NIR, and SWIR) of the EM spectrum. As it is emitted by objects with much cooler temperatures than the sun, EM radiation from the thermal emissive portion of the EM spectrum has other mechanisms which are not depicted in Figure 2.4, but those are outside the scope of this research, which focused solely on the solar reflective portion of the EM spectrum.

Path 1 depicts the direct solar irradiance component which is the part of the incoming light that reflects off of the object in the scene and is transmitted through the atmosphere to the sensor aperture. **Path 2** shows the contribution from the indirect solar irradiance, which is scattered by the atmosphere, reflects off the object, and is transmitted through the atmosphere to the sensor. **Path 3** shows the contribution from the solar irradiance which is scattered from a local object before reflecting off of the object of interest

and being transmitted to the sensor. **Path 4** shows the ground-scattered radiance which is scattered by the atmosphere (which possesses a Single-Scattering Albedo (SSA)), reflects off the object, and is transmitted to the sensor (the so-called 'adjacency effect, which plays an important role in two of our experimental setups). Finally, **Path 5** shows the upwelling path radiance which is scattered by the atmosphere directly into the sensor [8].

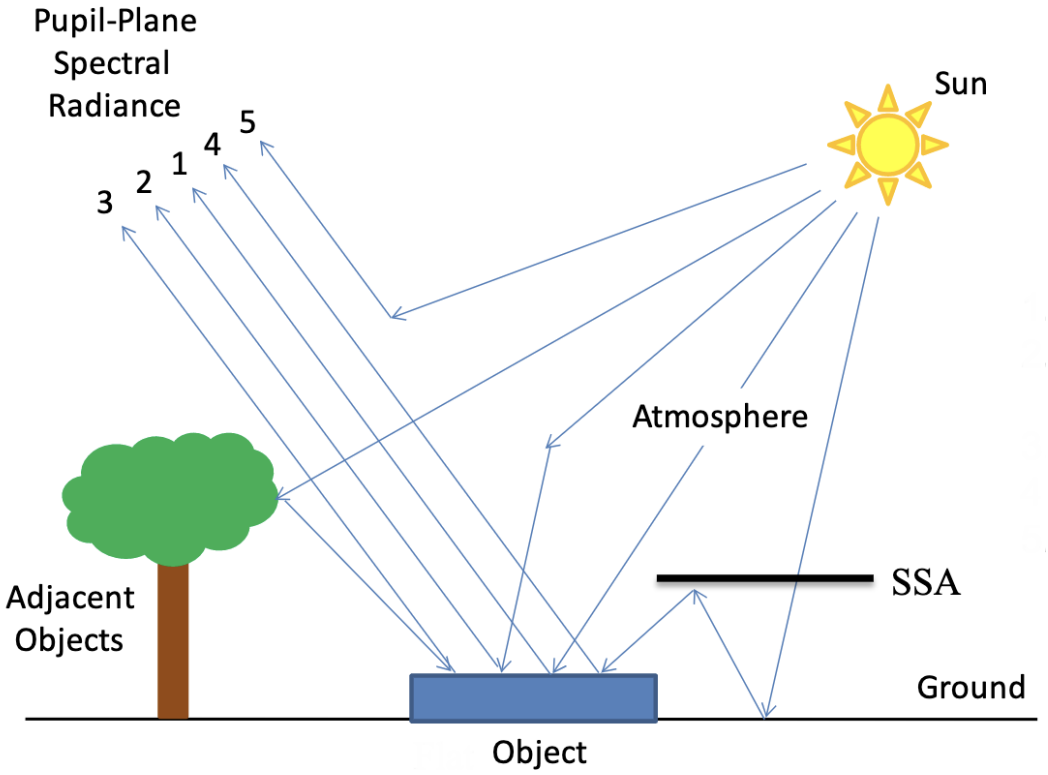

Figure 2.4: Radiative transfer methods for solar reflective part of the EM spectrum. Figure is used courtesy of Eismann [8].

Several models exist that accurately simulate the atmospheric effects

on remotely sensed radiation (often called RT modeling) One of these is the MODerate-resolution atmospheric TRANsmission and radiance (MODTRAN) code, which was developed and is maintained by Spectral Sciences, Incorporated [1]. MODTRAN uses a well-known differential equation which characterizes the transfer of solar radiation through the atmosphere and accepts a multitude of input parameters to accurately simulate the propagation of light from the VIS region to the LWIR region of the EM spectrum. Some of these parameters include the solar zenith angle, the atmospheric conditions (including visibility and haze conditions), and the temperature of the Earth. Both FASSP and DIRSIG utilize a MODTRAN plugin to describe atmospheric effects.

2.1.3 Imaging Spectrometry

HSI sensors are designed to accurately and precisely convert the at-sensor spectral radiance to a Digital Count (DC). This initial radiance-to-DC conversion is possible because of the onboard electronics of the HS sensor; the hardware required to complete this conversion will be the focus of this section. However, it should be noted that the DC signal does not need to be the final product of the sensor; this signal may be converted back to radiance by calibrating the sensor with respect to a source with a known radiance. In addition, the signal may also be converted from radiance to reflectance to compensate for the various impacts of the atmosphere that were discussed in Section 2.1.2. The techniques that exist to complete this conversion come in two flavors:

scene-based methods like the Empirical Line Method (ELM) and QUick Atmospheric Correction (QUAC), and physics-based methods like ATmospheric REMoval (ATREM) and Fast Line-of-sight Atmospheric Analysis of Spectral Hypercubes (FLAASH). Ientilucci and Adler-Golden provide a comprehensive outline of many of the existing the various atmospheric compensation techniques in their 2019 paper [19].

To capture data and convert the at-aperture radiance to some DC value, several hardware components are required; these are the scanning mechanism, the foreoptic (which focuses the light onto a spectrometer), the spectrometer, and finally, the focal plane array (FPA).

There exists two main types of scanning mechanisms in remote HSI. The whiskbroom scanning mechanism utilizes the sensor's forward motion and a rapidly-oscillating mirror to construct a three-dimensional hypercube of a scene. With this design, the FPA generally consists of either a single pixel, but may also consist of a row of pixels that is oriented in the direction of the platform's motion (along-track); while the platform moves forward, a mirror oscillates in a direction that is perpendicular to this motion (cross-track) to capture a two-dimensional image. While whiskbroom scanners were used in earlier HSI designs such as the Airborne Visible/Infrared Imaging Spectrometer (AVIRIS) [12] because of their ability to utilize a one-dimensional detector (a single detector element), the oscillating mirror component utilizes a moving component that is prone to breaking and requires regular maintenance.

The most prominent scanning mechanism used today is the pushbroom scanner. These mechanisms become more commonplace with the development of reliable two-dimensional Complementary Metal Oxide Semiconductor (CMOS) FPAs, which collect the spectra for a row of pixels simultaneously [8]. Unlike the whiskbroom design, the pushbroom FPA is oriented in the cross-track dimension and a two-dimensional image is created solely with its forward motion. Figure 2.5 depicts the manner by which an airborne pushbroom scanner creates a two-dimensional image.

Perhaps the most important component of the remote HSI sensor is its spectrometer, which separates out the spectrum of the incident radiance across the FPA. Spectrometer designs come in two main forms: dispersive prisms or diffraction gratings, which each carry their respective benefits and drawbacks and are useful in different regions of the EM spectrum.

Prisms are certainly the older design, and achieve angular dispersion of the incident light through their material properties. Prisms are able to confine energy from a monochromatic source of light to a constricted spatial band with minimal contamination from other wavelengths of light, and as a result, they don't require order filtering. However, prisms are limited in their resolving power, R, when compared to diffraction gratings in the VNIR region of the EM spectrum [8].

In contrast to the dispersive effect of prisms, gratings separate light through diffraction. To do this, gratings are designed with precise, periodic

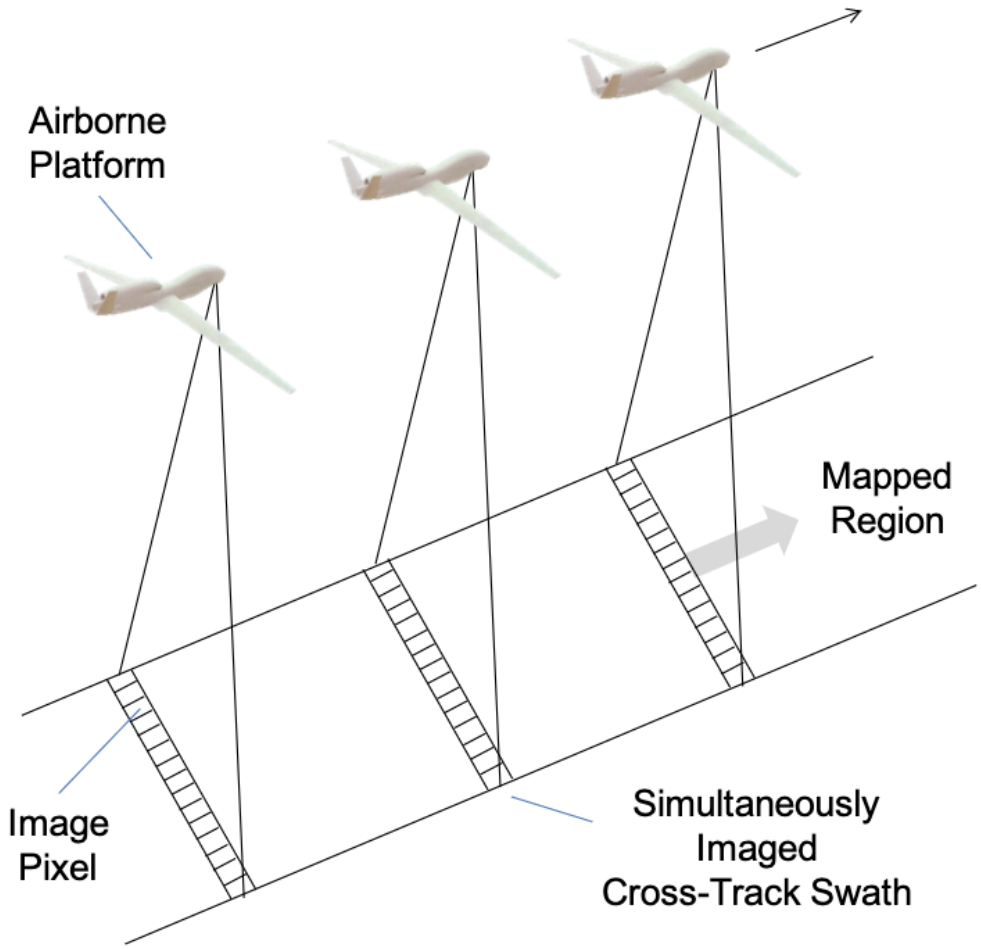

Figure 2.5: An airborne pushbroom scanner mounted on a drone captures the scene below. The pushbroom scanner forms a two-dimensional image by 'pushing' a one-dimensional array across the scene below. The one-dimensional array collects data from each projected pixel simultaneously. Figure is used courtesy of Eismann [8].

features to achieve resolving powers that are often larger than prisms. Due to the laws of diffraction, however, gratings mix different wavelengths of light,

and so the use of order-sorting filters is quite common to prevent contamination between different wavelengths of light. Gratings come in many different arrangements, with the Offner and Dyson designs being most popular in contemporary top-of-line HSI sensors [8]. The Headwall Nano-Hyperspec used in our experiments uses a Offner diffraction grating design to separate incident light into 272 bands, with each band possessing a width of approximately 2.2 nanometers (nm) [30]. The Nano utilizes a 2nd order filter to prevent order mixing.

The hardware components up to this point have collected, focused and separated out the incident radiation; the FPA is the component which actually converts this light into a quantized DC. FPAs generally come as a one- or two-dimensional array of pixels. One-dimensional arrays only allow for collection of spectral data for a single pixel at a time, and so are limited in their ability to capture spectral information for a large scene. As a result of this limitation, one-dimensional FPAs necessitated the use of the whiskbroom scanning mechanism. With improvements to the technology of two-dimensional FPAs, one-dimensional arrays have become less popular. Two-dimensional FPAs allow for the capture of spectral data for an entire row of pixels simultaneously. Figure 2.6 shows the basic two-dimensional FPA; spectral information for each pixel is mapped onto a column for that pixel (in the W_y dimension). The rows consist of individual pixels and run in the W_x dimension. FPA's are designed such that a central wavelength λ_0 falls on the center of the FPA at $y = 0$.

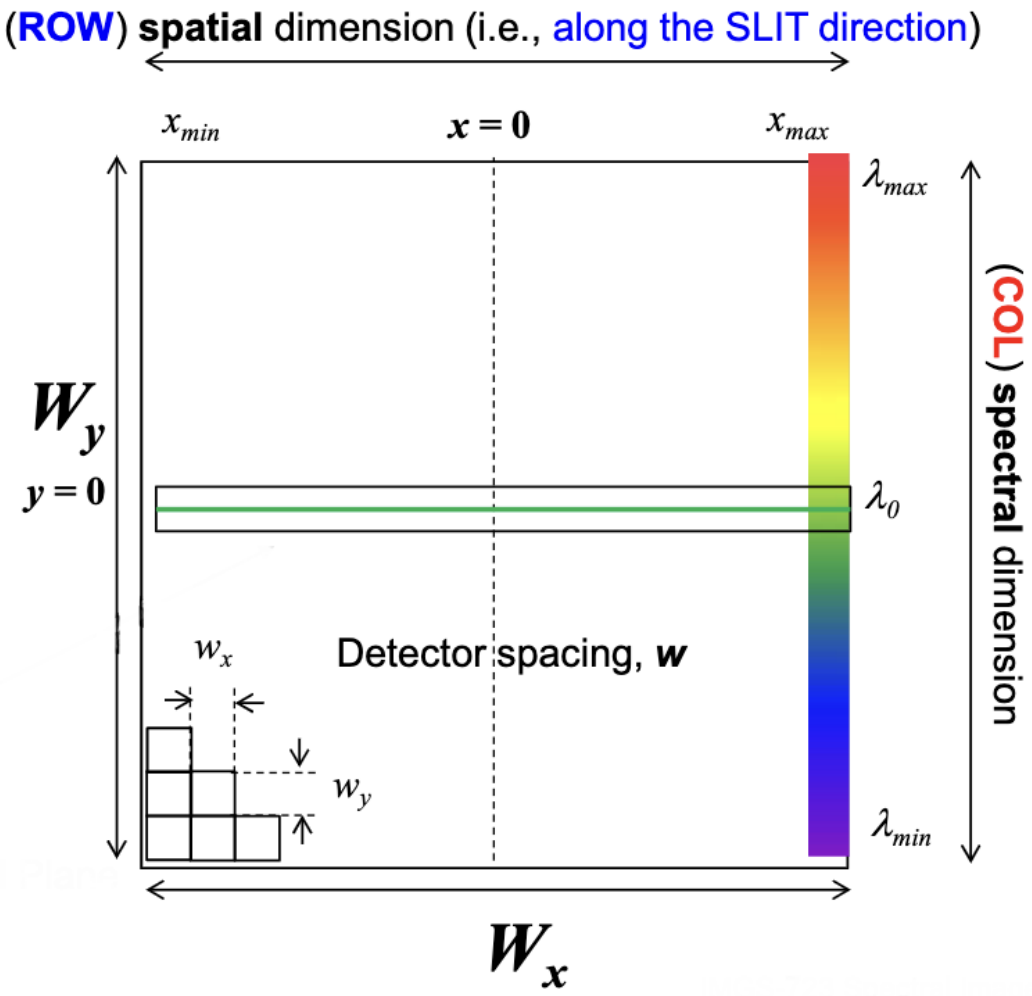

Figure 2.6: The basic layout of a two-dimensional FPA. The spatial dimension runs along W_x and the spectral dimension along W_y. Figure is used courtesy of Eismann [8].

As with any hardware component, FPAs suffer from imperfections (mainly in the form of optical aberrations). However, these can be, and often are, corrected for in either post-processing the data or by calibrating the

sensor itself [41].

2.1.4 Data Models

HSI data is often represented in two types of theoretical data models: statistical and geometric. Each of these models brings their own perspective of HSI data and make different assumptions.

For an HS sensor with k bands, the statistical data model represents HSI data as a multidimensional Gaussian Probability Density Function (PDF) with a mean vector, μ, and a symmetric covariance matrix $\mathbf{\Sigma}$ with size $k \times k$. In the covariance matrix, the diagonal represents the variance of each band with respect to itself while the off-diagonal values represent the covariance of each band with respect to the others.

The geometric data model represents each pixel in an HSI hypercube as a vector with each element in that vector as the spectral radiance at a specific wavelength; for a sensor with k bands, each pixel would look like $\mathbf{x}_i = [L_i(\lambda_1) \quad L_i(\lambda_2) \quad \cdots L_i(\lambda_k)]^T$, where i is the index of each pixel. Representing the data in this way creates allows each pixel to be visualized as a vector in a k-dimensional space. The geometric data model is the fundamental basis of the LMM, which is the theoretical foundation that I am seeking to test. In the geometric representation, if two pure materials ($\mathbf{x_1}$ and $\mathbf{x_2}$) are captured by a single pixel, a $(k-1)$-dimensional 'simplex' is formed. This simplex represents the theoretical boundary where any linear combination of

the two pure materials (called endmembers) would reside. This describes the foundation of Linear Spectral Mixing (LSM), which says that with pure linear mixing, the signal of a pixel (which captures a combination of two pure endmembers) may be represented as $\mathbf{x} = \alpha_1 \mathbf{x_1} + (1 - \alpha_1)\mathbf{x_2}$, where α_1 is the abundance of one of the endmembers. The statistical and geometric data representations of HSI data are the foundation on which the analysis of HSI data are performed. One of the most prominent types of analysis in the realm of HSI data is target detection.

2.2 Hyperspectral Target Detection

HS target detection aims to find objects of interest within HSI by utilizing those objects' spectral features. It is assumed that these targets are present relatively rarely in the scene. In HS target detection, it must be decided whether a given pixel, $\mathbf{x}$, contains the target spectrum or not: to do this, statistical hypotheses testing is used, with which a decision rule is applied to distinguish all pixels within an HSI data cube into either containing the target and the background, $\mathcal{H}_1$, or only containing the background, $\mathcal{H}_0$. Equation 2.3 shows these two decision rules.

$$\begin{aligned} x \in \mathcal{R}_0 &\Rightarrow \text{Accept } \mathcal{H}_0 \\ x \in \mathcal{R}_1 &\Rightarrow \text{Accept } \mathcal{H}_1 \end{aligned} \tag{2.3}$$

If decision rule $\mathcal{H}_0$ is chosen and the target is indeed absent from that pixel, it is a correct rejection; likewise, if decision rule $\mathcal{H}_1$ is chosen and the

target is present in that pixel, it is a correct detection. There exists, of course, error the ability to determine if a pixel contains the target or not. These errors come in two types: **Type 1** and **Type 2**. **Type 2** errors arise when a pixel is incorrectly classified as not containing the target when it actually does (a miss) and **Type 1** errors occur when we classify a pixel as containing the target when the target is not present (a false alarm). There exists several theoretical decision rules to suit different applications. The *Neyman-Pearson* (NP) criterion seeks to minimize the probability of false alarms (P_{FA}) while maximizing the probability of successful detections (P_D). By utilizing the NP criterion the user may determine what an acceptable P_{FA} is and make it constant (a so-called Constant False Alarm Rate (CFAR)).

In a graphical sense, it is possible to envision the distribution of pixels into two sets of Gaussian or near-Gaussian PDFs, where one PDF corresponds with the background pixels and the other with the target pixels. Figure 2.7 shows this depiction. The total P_{FA} may be calculated by integrating the area right of the NP criterion, (η), of the $\mathcal{H}_0$ PDF; the total P_D may be calculated by integrating the area right of η of the $\mathcal{H}_1$ PDF.

This trade off between P_D and P_{FA} may also be depicted in a Receiver Operating Characteristic (ROC) curve, in which, the P_D is plotted on the vertical axis and P_{FA} is plotted on the horizontal one; both are on a normalized scale. Oftentimes with HSI data, the P_{FA} is shown on a logarithmic scale. The ROC curve is commonly-used method to depict HS detector performance.

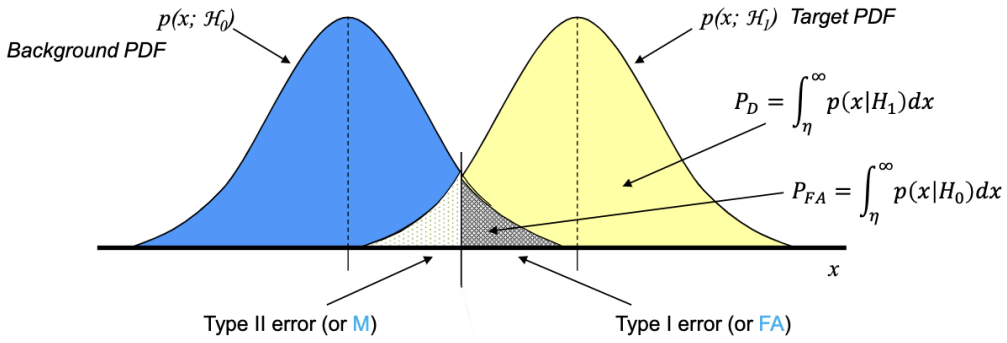

Figure 2.7: A graphical depiction of the hypothesis testing discussed above. The left PDF above corresponds to the background pixels while the right PDF corresponds to the target pixels. The critical threshold may be set by the user; with the NP criterion, it is set to an acceptable, constant value. Figure is used courtesy of Eismann [8].

To determine whether a pixel actually contains a target or not, a user-defined 'truth mask' must be created, in which the user clearly delineates which pixels actually contain the target and which do not. The art of defining truth masks can be subjective, and as a result, two users may define two different truth masks which will result in different ROC curves, even with the same data and target spectrum.

2.2.1 Relevant Target Detection Algorithms

Having discussed the theoretical basis of HS target detection, a brief overview of some of the relevant HS target detection algorithms will be given. These algorithms may be broken down into two basic categories: full-pixel and sub-pixel. For the purposes of this thesis, we will focus on the sub-pixel algo-

rithms and specifically on those that are based on the stochastic background models. These stochastic models assume that the spectrum of each pixel may be represented as a vector in k-dimensional space (for an HS sensor with k bands) and that the variability of these spectra may be modeled as multivariate probability distributions [26]. The relevant algorithms that will be discussed here are the Adaptive-Cosine Estimator (ACE), the Constrained Energy Minimization (CEM) algorithm, and the Spectral Angle Mapper (SAM) algorithm. Note that all of these algorithms compute normalized scores for every pixel which grade the likelihood of each pixel in the HSI data possessing the target. Only results from the CEM algorithm are shown in Section 4.3 of this thesis.

The ACE algorithm models the variability of the background pixels (those not containing the target) using a mean vector, $\mu_{\mathbf{b}}$, and a covariance matrix, Σ_b, and the known target spectrum as a vector, $\mathbf{s}$. In HS target detection, it is common for the mean and covariance values of the background pixels are estimated from the HSI data while the target spectrum is often found from a known spectral library [26]. Equation 2.4 shows the ACE algorithm, where $\mathbf{x}$ is the pixel spectrum being tested. Note that in every instance of $\mathbf{s}$ and $\mathbf{x}$ in Equation 2.4, the mean of the background spectra, $\mu_{\mathbf{b}}$, is subtracted off.

$$r_{ACE}(\mathbf{x}) = \frac{[(\mathbf{s}-\mu_{\mathbf{b}})^T\Sigma_b^{-1}(\mathbf{x}-\mu_{\mathbf{b}})]^2}{(\mathbf{s}-\mu_{\mathbf{b}})^T\Sigma_b^{-1}(\mathbf{s}-\mu_{\mathbf{b}})(\mathbf{x}-\mu_{\mathbf{b}})^T\Sigma_b^{-1}(\mathbf{x}-\mu_{\mathbf{b}})} \tag{2.4}$$

The CEM algorithm relies not on the covariance representation of the background pixels, but on the correlation, R. It is especially important to the purposes of this thesis, as it is one of the primary algorithms used in the processing of FASSP. Equation 2.5 depicts the CEM algorithm.

$$r_{CEM}(\mathbf{x}) = \frac{(\mathbf{s}-\mu_\mathbf{b})^T\mathbf{R^{-1}}(x-\mu_\mathbf{b})}{(\mathbf{s}-\mu_\mathbf{b})^T\mathbf{R^{-1}}(\mathbf{s}-\mu_\mathbf{b})} \tag{2.5}$$

The SAM algorithm is magnitude-invariant which means that it treats 'bright' signals the same as it does 'dim' ones; to find targets in HSI data, it only compares the shape of a pixel's spectrum to that of a known target spectrum. To do this, SAM computes the angle between the two k-dimensional spectra. This is shown in Equation 2.6. Note that SAM produces smaller values for those pixels which appear more similar to the known target spectrum and larger values for those that appear more dissimilar [8].

$$r_{SAM}(\mathbf{x}) = \arccos[\frac{(\mathbf{s}-\mu_\mathbf{b})^T(\mathbf{x}-\mu_\mathbf{b})}{\sqrt{((\mathbf{s}-\mu_\mathbf{b})^T(\mathbf{s}-\mu_\mathbf{b}))((\mathbf{x}-\mu_\mathbf{b})^T(\mathbf{x}-\mu_\mathbf{b}))}}] \tag{2.6}$$

Only the CEM algorithm was utilized for this research; its application will be discussed in more detail in Section 3. A more comprehensive explanation and list of HS target detection algorithms has been explored by Manolakis and Shaw [26].

2.3 Modeling Software

To accurately model the challenges facing HSI in remote sensing tasks, software has been developed to understand and predict sensor performance. Among these (and pertinent to this research) is the Digital Imaging and Remote Sensing Image Generation (DIRSIG) developed by the Digital Imaging and Remote Sensing (DIRS) group at the Rochester Institute of Technology's Carlson Center for Imaging Science [11]. This program utilizes atmospheric modeling data from MODTRAN, which itself was created by Spectral Sciences Incorporated [1]. The current iteration of DIRSIG, DIRSIG5, allows for custom scene generation with accurate reflectance statistics and synthetic data generation for many different sensing modalities.

Another program is the Forecasting and Analysis of Spectroradiometric System Performance model (FASSP). Unlike the path-tracing paradigm of DIRSIG, FASSP relies on the LMM as the foundational model in its computations. As mentioned in Section 1.2, FASSP was first developed by Dr. John Kerekes and Jerrold Baum and introduced in their 2002 paper [23, 24]. FASSP uses statistical reflectance and emissivity characteristics of a scene, which it then propagates through the atmosphere (which is described using user inputs) to a user-defined sensor, where various results are generated to illustrate target detection performance. FASSP is especially adept at generating ROC curves and predicted target radiances. DIRSIG and FASSP are explained more in their respective subsections below.

2.3.1 DIRSIG

DIRSIG utilizes a unified path-tracing method to generate a three-dimensional simulation environment that is capable of synthetically generating data for various sensing modalities [11]. Its development began in the 1990s; DIRSIG5 is the latest iteration of the program and currently possesses the capability to generate datasets for hardware trade studies and algorithm performance analysis in a multitude of operating regimes (including Multispectral Imaging (MSI), HSI, LIght Detection and Ranging (LIDAR), and Synthetic Aperture Radar (SAR)). DIRSIG5's path-tracing method constructs the path of light backwards from a sensor aperture, through a scene, and back to its source (i.e. the sun), or to a terminating event (i.e. being absorbed in the atmosphere).

Generating a scene in DIRSIG requires a scene model which incorporates the geometry of objects within a scene. For an urban scene, for example, this would involve constructing three-dimensional polygon objects for the buildings; these objects can then be instanced within the scene at specific locations and times. The scene model also incorporates an optical description of the materials present within the scene. These material properties can include spectral reflectance, emissivity, and transmission descriptions, BRDFs, and thermodynamic characteristics. The material properties can then be associated with the three-dimensional geometry to describe specific facets. In addition, DIRSIG supports a variety of tools that can take MSI or HSI data

and utilize the spatial and spectral characteristics of this data to project it onto a scene's geometry.

DIRSIG also relies on a sensor model, which utilizes a description of a remote sensor to determine what the scene would 'look like' to that sensor. This model is platform-centric, meaning that FPAs are attached onto a vehicle with a defined location and motion. The FPAs may be defined with a variety of independent characteristics, including Spectral Response Functions (SRFs), Point Spread Functions (PSFs), band descriptions, 'unprogrammed motion' (like platform jitter), and sensor response. DIRSIG also incorporates data from MODTRAN to compute the atmospheric effects on the final product [11].

DIRSIG utilizes various plug-ins, which can be enabled to use various features (hopefully for increased simulation accuracy). Some of the most important relevant to this research are:

1. **MODTRAN plug-in**: allows for user descriptions of accurate modeling of the atmosphere scattering and absorption

2. **Solar and Lunar Ephemeris plug-in**: allows for user descriptions of temporally-static or dynamic scenes with time-specific illumination conditions

3. **FASSP plug-in**: allows for the incorporation of FASSP sensor descriptions, which is incredibly pertinent to our DIRSIG and FASSP data

comparisons (more will be given on this in Section 3.2.2)

These plug-ins work in coordination with each other: for example, the Solar and Lunar Ephemeris plug-in would take as an input as user-defined time and date, calculate the resulting solar and lunar zenith and azimuth angles, and use that to inform the MODTRAN runs, and thus the atmospheric conditions.

In addition to these plug-ins, the **ClassicEmissivity** model was utilized to include a simple description of the Treeshine Reflector (TR) panel BRF in the DIRSIG simulations. This model takes as an input a '.ems' file type and utilizes a simple scalar quantity to describe how specular a material is. Section 3.2.2 describes the work with this model in more detail.

2.3.2 FASSP

FASSP was first developed to enhance remote sensor system design and functionality [23]. It is an end-to-end analytical model that takes as inputs a description of the scene, the sensor parameters, and the desired processing settings. Using these inputs, FASSP uses statistical models to predict detector performance by applying analytical equations [23] that utilize the core assumptions of the LMM. FASSP is specifically adept at modeling the detection of sub-pixel targets in a multi-background scene. Figure 2.8 depicts a block diagram of the FASSP modeling software. The diagram shows the computations performed on the spectral mean and covariances from the scene description as they are propagated to the sensor model, and finally, to the processing model.

The model can most simply broken down into three components: the scene, the sensor, and the processing.

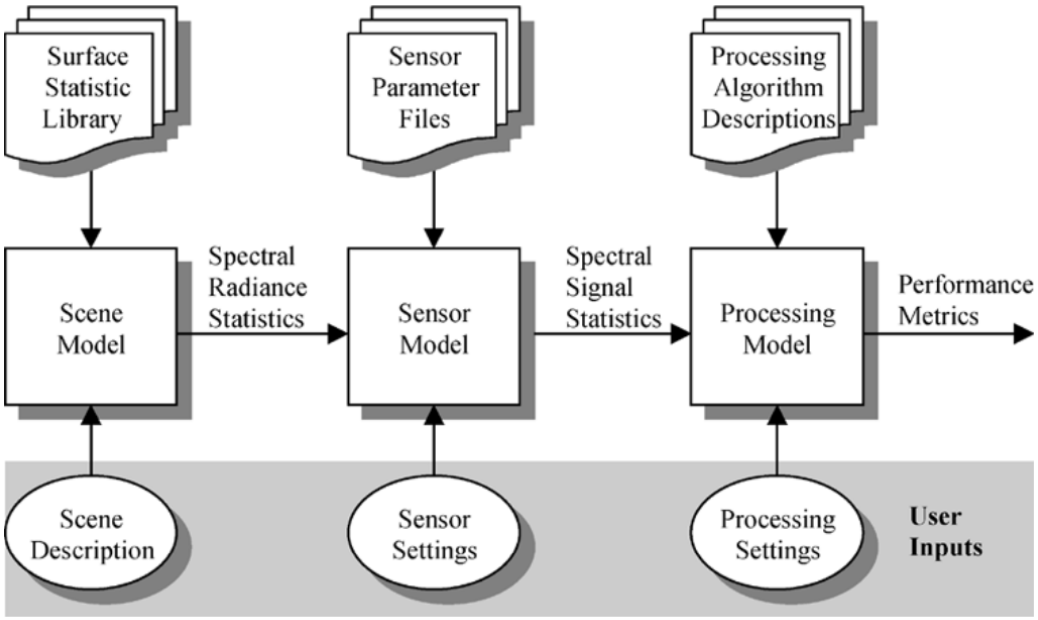

Figure 2.8: Block diagram of the FASSP modeling software which shows the flow of spectral mean and covariances from the scene model to the sensor model, and finally, to the processing model. Figure is used courtesy of Kerekes and Baum [23].

The scene model consists of a single target class and M background classes. The user inputs a proportion of the scene filled by each background class and the fraction of a pixel filled by the target class ($0 < f_T \leq 1$) that possesses a direct line-of-sight to the sensor. Another user input, $0 \leq f_S \leq 1$, denotes how much of the target is covered by shadow. If $f_S > 0$, the fraction of the sky's hemisphere that is fully visible from the target, f_{sky} must also

be specified. These shadowing variables allow for the specification of a scene where the downwelling sky irradiance on the target is partially blocked. In this situation, the amount of diffuse radiance on the target is reduced proportionally by f_{sky}. FASSP assumes that the target is somewhere in one of the background classes, which is denoted m^* to differentiate it from the other background classes. Each of these classes is described by their first and second-order spectral reflectance statistics: their means and variances. FASSP assumes a simple area-weighted LMM for the sub-pixel target and does not simulate a specific spatial layout.

To accurately describe the target and background classes, spectral reflectance statistics must be provided for each class. These statistics consist of a spectral mean reflectance vector ρ and a reflectance spectral covariance matrix, Σ_ρ of size $K \times K$. FASSP assumes that the reflectance distribution of each background or target is unimodal, and as a result, it is sometimes necessary to break up individual background classes with more than one mode into multiple classes to ensure unimodal behavior. FASSP uses MODTRAN to compute atmospheric effects for each of the M background classes and also for the total scene average.

FASSP computes the mean spectral radiance and spectral radiance covariance matrices for each of the M background classes. FASSP also computes the mean and covariance radiance for the target class. It should be noted that the calculations that FASSP does to compute the mean spectral radiance for

either the fully-illuminated target or for the target which is either partially or fully shadowed are different so that it can better consider the impact of shadowing and the reduction of illumination from that portion of the sky in its calculations.

The FASSP sensor model takes as an input the spectral radiance statistics that were computed from the scene and applies sensor effects to produce a form of the scene that would be imaged by an MSI or HSI sensor. These sensor effects include radiometric noise and the sensor spectral response. The radiometric noise calculations include calculations for total detector noise, which are scaled by a user-specified noise factor g_n before being added to the diagonals of the spectral covariance matrices; they also include the relative calibration error, quantization noise to account for errors in the analog-to-digital conversion. The Signal-to-Noise Ratio (SNR) is then calculated for each of the background classes and the target class [23].

The final component of the FASSP modeling software is the processing model. There are three facets of the processing model: atmospheric compensation, feature selection, and performance metrics. The user has the option to determine whether they want the spectral radiance output from the sensor model to be atmospherically compensated for via the ELM discussed in Section 2.1.3.

Within the feature selection, the user also has the option to specify whether they want to include all bands or reduce them to avoid specific spectral

regions (like water absorption bands), whether they want to utilize principle components via eigenvector decomposition, and whether they want to average bands in order to simulate a MSI sensor.

There exists three algorithms to determine the performance of the sensor at the subpixel target detection task: Spectral Characterization Accuracy (SCA), the target detection performance (as a result of applying one of the target detection algorithms discussed in the Section 2.2.1) and total error. The SCA measures how well the spectral reflectance can be retrieved from the sensor data and is calculated as the mean difference between the computed surface reflectance and the known reflectance; the SCA also includes the standard deviation for each spectral channel as well.

To graphically show target detection performance, FASSP generates ROC curves by plotting the P_Ds versus the P_{FA}s. To generate ROC curves, FASSP has several options for target detection algorithms: the one important for the scope of this thesis is the Constrained Energy Minimization (CEM) algorithm. FASSP assumes that the output of these algorithms is a normally-distribution, which is generally justified by the Central Limit Theorem when there exists a large enough number of random variables.

The total error metric approximates the total error as $P_e \approx \frac{1}{2}(1-P_D)+\frac{1}{2}P_{FA}$ when there exists a two-class equal *a priori* probability case. It serves as a single scalar that can be utilized for relative performance comparisons and does not distinguish between errors that are due to false alarms or missed

detections [23].

As mentioned in Section 1.2, FASSP has been validated in several studies, including with data from a collection performed with the Hyperspectral Digital Imagery Collection Experiment (HYDICE) sensor in 1995 [32], in which it predicted mean spectral radiance curves to within 5% to 10% of the measured values. Additional information on FASSP can be found in Kerekes' and Baum's 2002 and 2005 papers [23, 24].

Chapter 3

Methods

In this Chapter, the design of the testing setups used in the September 2022 Tait Preserve data collect and the methods used to process the resulting experimental data, as well as the data from FASSP and DIRSIG will be explained.

3.1 Tait Preserve Testing Setup

In order to test the impact of nonlinear effects on the LMM, four testing setups were designed in order to collect empirical data with the Headwall Nano-Hyperspec HSI sensor at RIT's Tait Preserve in Rochester, New York on September 9, 2022. Figure 3.1 shows two views of Tait Preserve from a DJI Mavic.

The left image is more zoomed-out and shows the main building as well as a gardening area, some fields, and the adjacent lake. The red square in this image is the area of interest and is shown more closely in the right image. The right image shows the base setup, which includes the five green sub-pixel targets placed on the gravel, as well as some felt panels below that and two

Figure 3.1: Two views from above of Tait Preserve on the day of our data collect from a DJI Mavic. The left image is more zoomed-out; the right image shows a close-up (deliminated by the red box in the left image) of the first of the four experimental setups: the base setup.

permaflect panels above them. The other three experimental setups were all variations of this one, incorporating additional panels which either shadowing or spectrally contaminated the green sub-pixel target panels.

Each of these setups included five sub-pixel targets that were designed to have specific pixel fill fractions (FF) for a GSD of approximately 4.5 centimeters. The targets were designed to have FF of 100%, 80%, 60%, 40%, and 20% and measured 45.28 inches by 33.71 inches, with the exception of the 100% target, which measured 3 foot by 4 foot. The sub-pixel targets were painted green on one side and gray on the other; only the green side is relevant to this thesis. These novel targets were designed and constructed by Chase Cañas and are an enlarged version of an earlier design [6]. A close-up of the

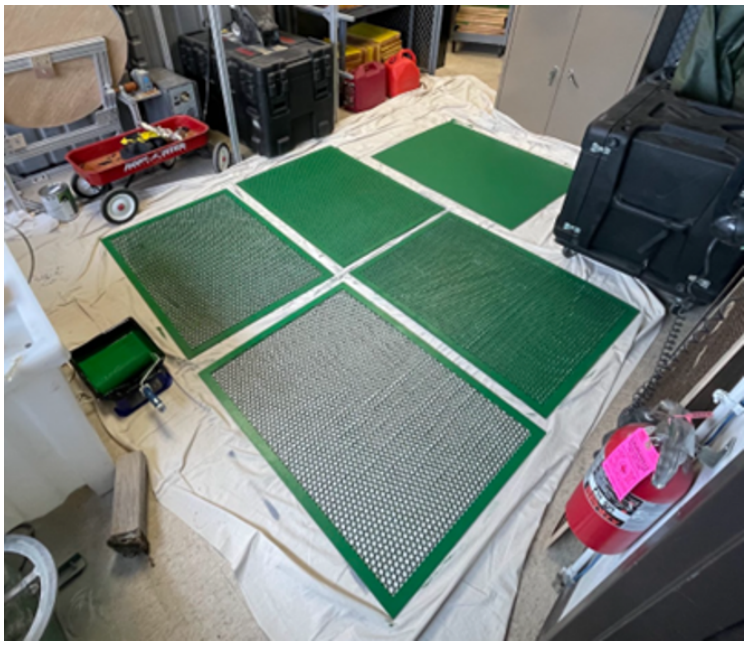

Figure 3.2: The five subpixel FF targets designed by Chase Cañas and constructed by he and Colin Maloney in September 2022 prior to the data collect.

targets after painting are shown in Figure 3.2.

In addition to these targets, two sets of five panels were constructed from Oriented Strand Board (OSB) to provide the desired nonlinear effects. The first set of panels were Shadowing (S) panels and were designed to be stood up vertically in order to shadow the entire area of the sub-pixel targets. The second set of panels constructed were the Treeshine Reflector (TR) panels which were painted a bright red color. A semi-matte paint was chosen in an attempt to reduce the specular nature of the TR panel and to increase the probability of producing spectral contamination in the detected spectra of the green targets. The intent with the TR panels was to contaminate the spectra

Figure 3.3: The four target setups used at Tait Preserve for the data collect. The top-left image shows the base setup of green sub-pixel targets with no shadowing or TR panels. The 20% FF target is closest in the field-of-view (FOV). The top-right image shows the shadowing panel setup. The bottom-left image shows the TR panel and shadowing panel (TR-S) setup. The TR panel setup is shown in the bottom-right image. The spectral contamination from the TR panel may be seen on the shadowing panel in the bottom-left image.

of the green targets, much like tree leaves and vegetation often contaminate the spectra of objects near them (thus inspiring the term, the 'treeshine effect'). To accomplish this, the panels needed to reflect the direct and indirect components of light onto the target panels through both specular and diffuse means. All of these panels measured 4 foot by 4 foot; these dimensions were chosen for two reasons: to ensure that the shadowing panels were large enough to completely shadow the targeting panels with the predetermined solar zenith angle for the day the data collect would take place and also for ease of construction.

There were four testing setups designed using the TR panels, the shadowing panels, and the sub-pixel targets. These setups are shown in Figure 3.3, which depicts a ground-level view of the four setups on the day of the collect.

1. **Base Setup**: Green sub-pixel targets laid out on gravel
2. **Shadowing Panel Setup**: Shadowing panels were placed to fully shadow the green targets
3. **Treeshine Reflector and Shadowing Panel (TR-S) Setup**: Shadowing panels were left in place and TR panels were set up on opposite side of target
4. **Treeshine Reflector (TR) Setup**: TR panels left in place and shadowing panels were removed, allowing targets to be in direct solar illumination again

With the experimental design process of the work completed, the drone flights at Tait Preserve were completed on September 9, 2022. Eleven drone flights were completed in total, but only the four with the described setups were relevant to this thesis. The sensor that was used to collect all of the HSI data was the Headwall Hyperspec Nano, which possesses 272 bands covering the EM spectrum from approximately 400 nm to 1000 nm. The weather on the day of the data collect was very clear and sunny; towards the latter end of the missions, however, some clouds began to arrive and so flights were timed when the sun was not blocked.

The flights were all conducted from 10:31 to 13:30 Eastern Time (ET), during which time the solar zenith angle ranged from approximately 46° to 53°. As the sun moved in the sky (and the projected shadows from the shadowing panels changed), it become necessary to rotate the sub-pixel targets so that they continued to be shadowed to the greatest extent possible throughout the various target setups. This rotation is visible in the top right, bottom left, and bottom right images of Figure 3.3. One consequence of the design of the sub-pixel targets, however, was that the predetermined target FF could be obtained no matter how the targets are rotated, so this slight rotation throughout the day shouldn't have impacted our data substantially.

As mentioned above, the TR panel was painted with a matte paint and with a paint roller with a $\frac{1}{2}$-inch nap so as to ensure that it was successful in contaminating the spectrum of the adjacent sub-pixel targets. However, when

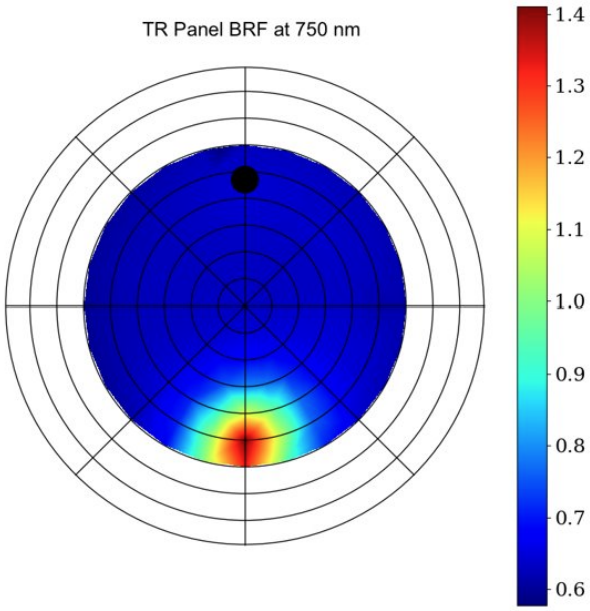

Figure 3.4: The BRF of the Treeshine Reflector (TR) panel which shows that the TR panel is largely 'specular'; this behavior is evidenced by the region of large reflectivity (the bright red, yellow, and green area) on the bottom of the diagram, where light is reflected in accordance with the law of reflection [8]. On this diagram, the light source was placed where the black circle is on the center top. Note that the BRF is a unit-less quantity.

it was noticed that the TR panel appeared to be quite specular on the day of the data collect, the plan was made to quantify the specular nature of the TR panel Bi-directional Reflectance Factor (BRF) using RIT's goniometer (GRIT-T), which was discussed above in Section 2.1. These measurements were performed with a light source placed at 46.7° above the horizon, which

was what the solar zenith angle was approximately 11:30 ET, when the TR-S setup was being imaged in our drone flights.

As shown in Figure 3.4, the measured BRF of the TR panel shows that it still possessed a large specular lobe. This figure shows the BRF measured at 750 nm, which was representative of the panel's behavior at all wavelengths from 400 nm to 2500 nm.

The BRF is a measurement that is similar to the BRDF discussed in Sections 1.2 and 2.1.1. It is defined as the ratio of the measured spectra defined by the spectra that would have been measured from a perfectly Lambertian surface; as it is defined as the ratio of two radiances, it is a unit-less quantity. The specular nature of the TR panel may also be seen in the TR-S and TR setups of Figure 3.3.

In addition to the collection of HSI data, a HR-1024i field spectrometer from Spectra Vista Corp (SVC), was used to collect 'ground truth' spectral data for all of the target panels, as well as colored felt panels and Spectralon panels, and many of the other materials in the scene (the gravel, grass, concrete, and metal and wood docks nearby). The SVC measures spectral radiance; the reflectance is obtained by ratioing the measured radiance to a 'known' Spectralon calibration panel. This data was collected with a 4 deg lens. Figure 3.5 shows some of the SVC measurements of felt panels from the day of the data collect from various felt panels that were placed on the gravel path at Tait Preserve for calibration purposes.

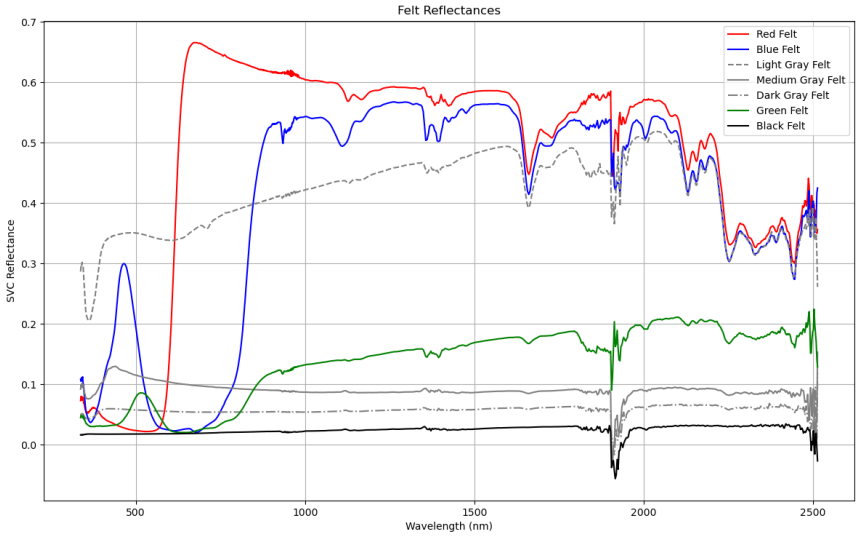

Figure 3.5: Some of the measured reflectance spectra from the felt panels nearby the targets in our September data collect. These measurements were taken by the HR-1024i field spectrometer from the SVC.

3.2 Data Processing Paradigms

The goal in processing the data from each of data sources (experimental, FASSP, and DIRSIG) was to process the data in such a way as to have as comparable results as possible from each source. To do this, the operations of FASSP were emulated in the processing of our DIRSIG and experimental data processing to the greatest extent possible. This is because altering the operations of FASSP (which are mostly done 'under the hood', and as such, are somewhat inaccessible) was seen as excessively laborious and not conducive to the successful completion of the objectives of this research. Only by closely

aligning the data processing techniques could reasonably-comparable results be obtained.

This thesis aimed to produce two main types of results for comparison: target radiances and target detection performances in the form of Receiver-Operating Characteristic (ROC) curves. Both of these results, and the high-level methods to obtain them from each data source are shown in Figure 3.6. These types of results were chosen for two main reasons: both are good indicators of model performance in predicting sub-pixel target detection performance and both are produced by FASSP without any requisite processing. The target radiances indicate the accuracy of the LMM-based model (FASSP) and the path-tracing model (DIRSIG) in predicting what the spectrum of the green

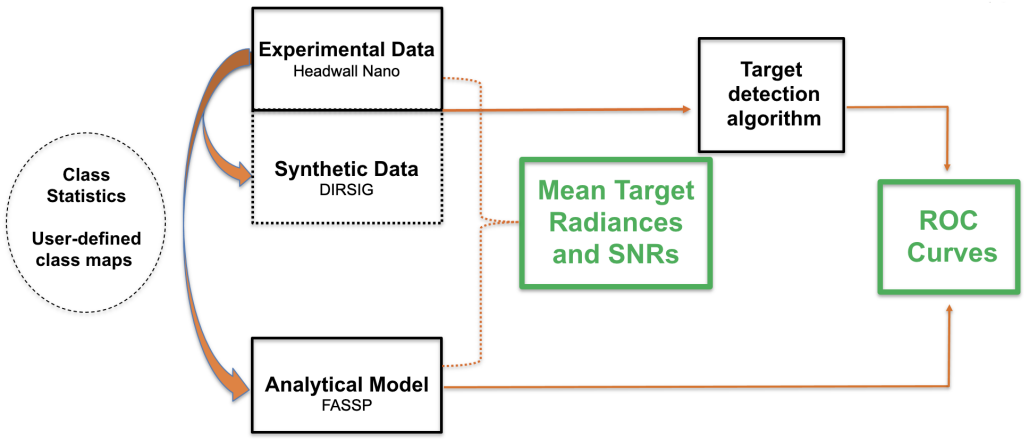

Figure 3.6: Data workflow from the three sources. In contrast to the raw data that was collected from the data collect and DIRSIG, most of FASSP's operation are completed under the hood, and as such, the results shown in Chapter 4 were produced automatically.

target 'looks like' to the sensor. These predictions can also be compared to the empirical results - that is, what the Headwall Nano detected on the day of the data collect. On the other hand, the ROC curves quantify the models' accuracy at predicting target detection performance.

As mentioned in Section 2.2, the target detection algorithm that was utilized in the processing of the Experimental and DIRSIG data was the Constrained Energy Minimization (CEM). The CEM was chosen because it is an oft-used measure of detection performance and it is already coded up in FASSP.

For all of the data sources, the target detection performance analysis was performed in the reflectance domain with the target spectrum taken as the average of the 100% green target ROI from the base setup from each data source. The transformation to the reflectance domain was performed in a unique manner for each data source.

For FASSP, this was computed under the hood using its internal processes which will not be explored in depth here but can be found in [23]. For the experimental data, the Headwall Nano's in-house calibration process was used to convert from raw DCs to reflectance. This process utilizes a 1-point ELM process with a single panel (with known radiance and reflectance) that is imaged prior to each flight. Re-sampling and geo-rectification of the data was also completed prior to any processing. This process was also used to convert the experimental DCs to spectral radiance. The DIRSIG data genera-

tion process utilized a new plug-in created by Scott Brown of DIRS, called the 'FASSP plug-in'. Generating synthetic data with this plug-in did not follow conventional DIRSIG practices, and as a result, only raw DCs were produced out of DIRSIG. To convert these DCs to spectral radiance and reflectance, the linear relationships (least-squares parameters) between the experimental DCs and radiance and reflectance were produced for each of the four setups and used to convert the DIRSIG DCs to reflectance and radiance for comparison. This process will be detailed more in Section 3.2.2.

It is important to note, that as a result of atmospherically compensating

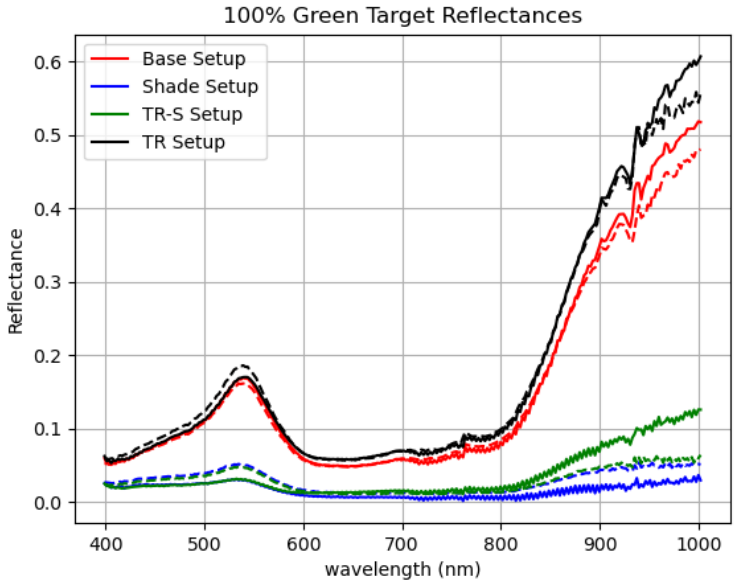

Figure 3.7: Average spectral reflectances of 100% green target ROI from DIRSIG data (dashed lines) and experimental data (solid lines) for each of the four setups.

all of our data in the manner that we did, although we did compensate the pixels belonging to the sub-pixel targets in the three setups with nonlinear effects (the shadowing panel setup, the TR-S panel setup, and the TR panel setup) in the same manner as those target pixels in the base setup, we should *not* have if we were aiming to achieve optimal target detection performance. These pixels experience different illumination conditions compared to those in the base setup and so compensating them in the same way effectively deals them a bad hand - especially because the target spectrum used for each of the setups was the average of the 100% green target ROI from the *base setup* for each of the data sources.

A better way to compensate these pixels would be to take into consideration the unique illumination conditions they each experienced. In Section 1.2, one such method was described where LIDAR data was leveraged to determine pixel-specific solar and sky-loading scaling factors to adjust the compensation approach accordingly [18]. As mentioned, the intent of this work was on comparing the accuracy of the different methodologies (Experimental, FASSP, and DIRSIG data), not to optimize target detection performance.

Figure 3.7 shows the predicted target reflectances from DIRSIG (dashed lines) and from the experimental data (solid lines) for each of the four setups; from it, the reader can see just how much the average target reflectance of the 100% green target ROI changes for each of the setups, both in shape and in magnitude. Using the reflectance spectra shown by the red lines (base

setup) to find the other spectra is understandably not optimal and will result in reduced performance for our setups with imposed nonlinear effects.

3.2.1 Experimental Data Processing

Following the Headwall calibration process, there were three nearly-identical forms of our experimental data in different domains: DC, reflectance, and radiance. To process the experimental data from the data collect, truth masks were first generated in ENVI, an image processing program from L3Harris GeoSpatial Solutions, Inc. for each of the four experimental setups described above. These truth masks contained ROIs for each of the five sub-pixel targets, a guard region around these targets to prevent unnecessary false alarms, and 14 natural and man-made materials in the scene. These 14 materials are specified in Table 3.1. Due to some sampling differences between the DC/reflectance domains and the radiance domain, it was necessary to generate separate truth masks for each. As a result, six total truth masks (two extra for each the shadowing and TR-S setups where the tolerances were a bit tighter) were made.

The reflectance statistics from the Headwall Nano from the base setup for the 14 natural and man-made background classes and the single 100% green target class were used to inform its computations. As discussed in Section 3.2, the target spectrum was taken as an average of the 100% green target class: the target radiance results that will be shown in Section 4 are simply the

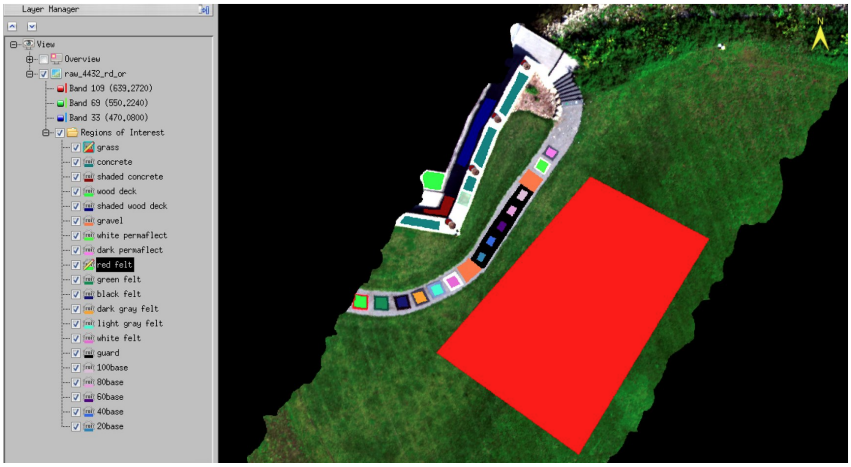

Figure 3.8: Screenshot in ENVI showing the base setup from the experimental data. Truth masks like this one were generated for the other setups. This screenshot shows the response from three bands of the Headwall Nano which approximations of a RGB sensor. 20 ROIs were specified for each setup: 5 for each of the sub-pixel FF targets, a guard region, and 14 others consisting of various man-made and natural materials in the scene. These are specified in Table 3.1.

average of this class from the radiance domain of experimental data.

There were a couple of extra steps to compute our target detection performance for the experimental results. To get the best comparison possible to the FASSP data processing (which will be discussed in Section 3.2.3, our target detection algorithm was not run over the entire HSI data cube; instead the truth masks that were created for the reflectance domain were used to create a new $1 \times N \times 272$ image chip where each of the N pixels was simply extracted from those ROIs discussed above. Then, the average background for each of the 272 bands was subtracted off of every pixel - these background

averages were also subtracted off of the target spectrum. When computing the score for the CEM algorithm, the correlation matrix, R, was then computed using the computation $R = x \cdot x^T$ and the inverse was calculated with the built-in NumPy matrix inverse tool (numpy.linalg.inv) and the score was computing using the equation given in Section 2.2.

From this, ROC curves were generated using the truth masks for each of the setups and by sorting the algorithm scores from most target-like to least target-like and comparing those pixels with the truth masks to determine whether the algorithm had successfully detected a target pixel (detection) or incorrectly assumed a target when only the background was present (false alarm). Area-Under-the-Curve (AUC) plots were also generated using the ROC curve data for an additional level of comparison between the three data types. Percent differences between the experimental data and DIRSIG and FASSP were also calculated for the mean target radiances and ROC curves.

3.2.2 DIRSIG Data Processing

The DIRSIG data processing methodology began with the construction of a three-dimensional scene of Tait Preserve. The final Tait DIRSIG scene contains three-dimensional geometry which describe the geography of the local area around where the sub-pixel targets were placed, reflectance statistics that describe the spectral properties of the many natural and man-made materials in the Tait area and their natural variation, an atmospheric model that closely

resembles that of the atmospheric conditions that were present when the data collect was conducted, and finally, a sensor model which is a relatively accurate approximation of the Headwall Nano. This process underwent many iterations to ensure accuracy with the experimental parameters and took approximately 7 months to work out all the bugs and ensure good spatial and spectral validation with the empirical data.

In the DIRSIG simulations, a description of the specular nature of the TR Panel was also included by utilizing the 'ClassicEmissivity' model. This model allowed for a description of the specular nature of the TR panel with a scalar value. In the DIRSIG simulations, this value was set to 0.9, indicating a highly specular panel that aligns with the measurements from the GRIT-T shown in Figure 3.4.

As a part of this development process, as mentioned in Sections 2.3.1 and 3.2, a new DIRSIG plug-in, the 'FASSP plug-in' was developed by Scott Brown to allow for an easy transfer of scene, atmosphere, and sensor descriptions from the pre-existing FASSP descriptions to DIRSIG. Figure 3.9 shows two screenshots of the FASSP sensor plug-in for DIRSIG. The left image shows a screenshot of some of the scene, sensor, and atmosphere parameters that are being inputted into DIRSIG to describe those conditions; the right shows a screenshot of the FASSP sensor description used to describe the spectral response and noise characteristics of the Headwall Nano. Of particular interest in the right image is the optical transmission variable column ('opt trans')

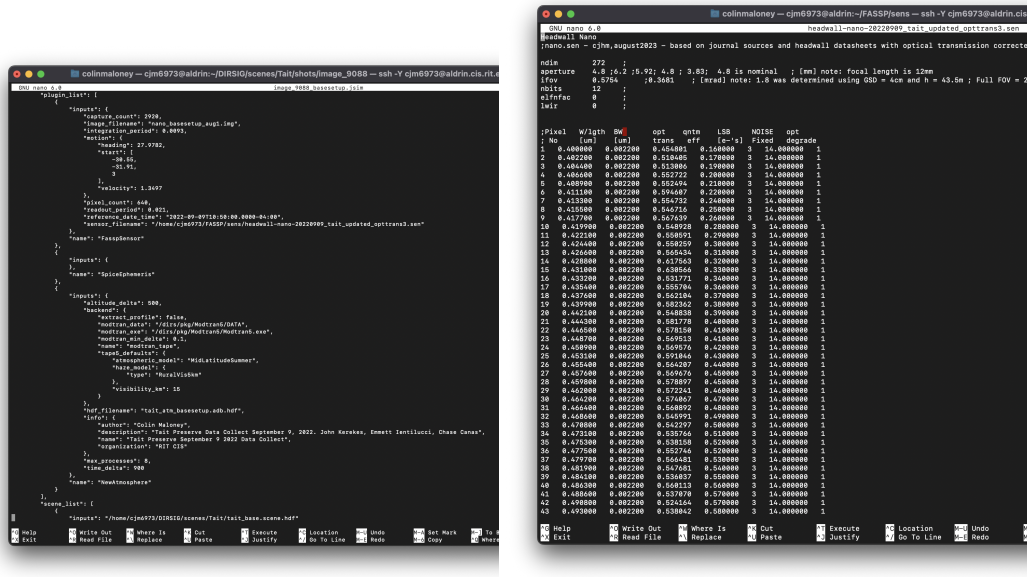

Figure 3.9: Two screenshots of the FASSP sensor plug-in used to inform the DIRSIG simulations. The left shows a screenshot of the scene, sensor, and atmosphere descriptions that are being inputted into DIRSIG for the base setup; the right shows a screenshot of the FASSP sensor description used to describe the spectral response and noise characteristics of the Headwall Nano. Of particular interest is the 'opt trans' column, which was updated to get an accurate approximation of the real Headwall Nano sensor.

which describes the spectral transmission of light in the sensor for every band.

The FASSP sensor plug-in enabled a simple transfer of the scene, sensor, and atmosphere descriptions to inform the DIRSIG computations. As a result of the novelty of the FASSP sensor plug-in, however, there did not exist a method to produce spectral radiances and reflectances out of DIRSIG. To transfer the raw DIRSIG DCs to the radiance and reflectance domains, a two-

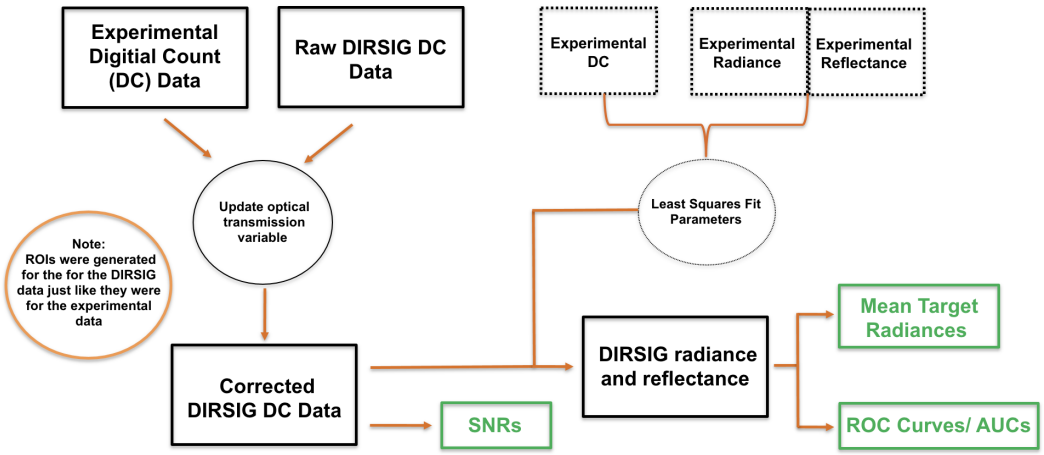

Figure 3.10: Workflow showing the process to generate comparable results for predicted mean target radiances, SNRs, and target detection performance (ROC curves and AUCs) from DIRSIG.

step process was utilized to ensure that it was as true to the experimental data as possible; in following this process, several assumptions were made. This data workflow process is shown graphically in Figure 3.10.

The first step in the DIRSIG data curation process was to check that the atmospheric model that was being used in DIRSIG closely emulated the conditions of the data collect. By utilizing the NewAtmosphere plug-in within DIRSIG and inputting the correct dates/times and predicted atmosphere transmission values (rural 5 km atmosphere model with 25 km visibility), the predicted atmospheric conditions were found to match up with the empirical ones. Note that these conditions were determined, in part, from FASSP through several iterations of testing.

Having ensured the correct atmospheric conditions, the predicted DIRSIG

DCs of a light gray felt panel in the Tait Scene were compared to the same felt panel in the experimental DC data. When this was done, it was observed that after subtracting off the Headwall Nano dark noise, DIRSIG predicted higher DCs at every wavelength than what evident in the experimental data. By making the assumption that DIRSIG should be producing the same DCs for this felt panel (in the base setup with no nonlinear effects), a simple 'ratio'-ing of the DIRSIG predicted DC of the light gray felt panel in the scene was used to update the optical transmission ('opt trans') variable of the Headwall Nano sensor description shown on the right image of Figure 3.9 which was informing the DIRSIG calculations. Upon doing this, it was possible to produce accurate predictions from DIRSIG for the various materials in the scene in the now-corrected DC domain.

Figure 3.11 shows four renderings from DIRSIG of the four experimental setups. These renderings were completed with a basic RGB sensor with only three bands to aid with visualization purposes, but with comparison to the experimental data, they also show the radiometric-accuracy that DIRSIG is capable of producing.

Figure 3.12 shows the full extent of the DIRSIG-generated base setup in ENVI in the DC domain. The sub-pixel targets, felt panels, and spectralon panels are visible on the gravel path, but note that the DIRSIG scene is rotated differently than the experimental data.

To convert from the corrected DC domain to radiance and reflectance, a

least squares fit conversion (slopes and offsets) between the experimental DCs and radiances and reflectances were used to convert the corrected DIRSIG DCs to radiance and reflectance. This method utilized four felt panels in the scene (white, light gray, dark gray, and black), which allowed for a high fidelity approximation of the linear relationships (slope and offset) between DCs and radiance and DCs and reflectance with which to convert the corrected DIRSIG

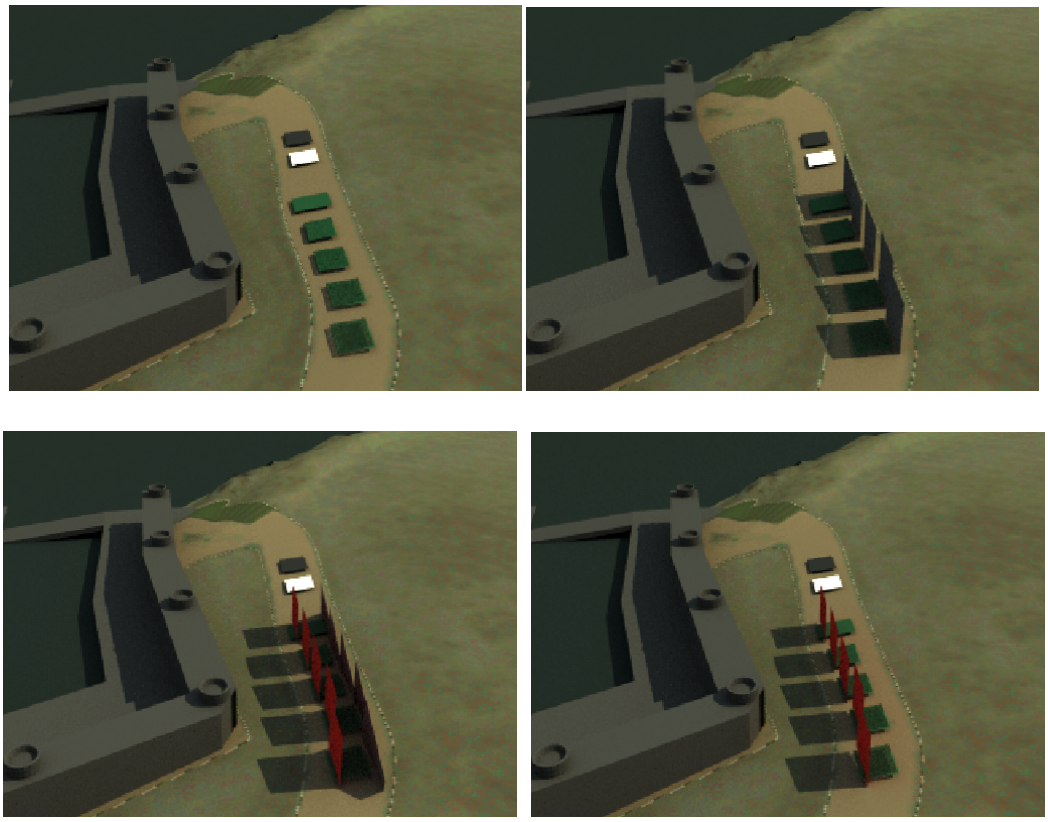

Figure 3.11: Screenshots showing a DIRSIG rendering of the four setups. Top left is the base setup, top right is the shadowing setup, bottom left is the TR-S setup, and bottom right is the TR setup.

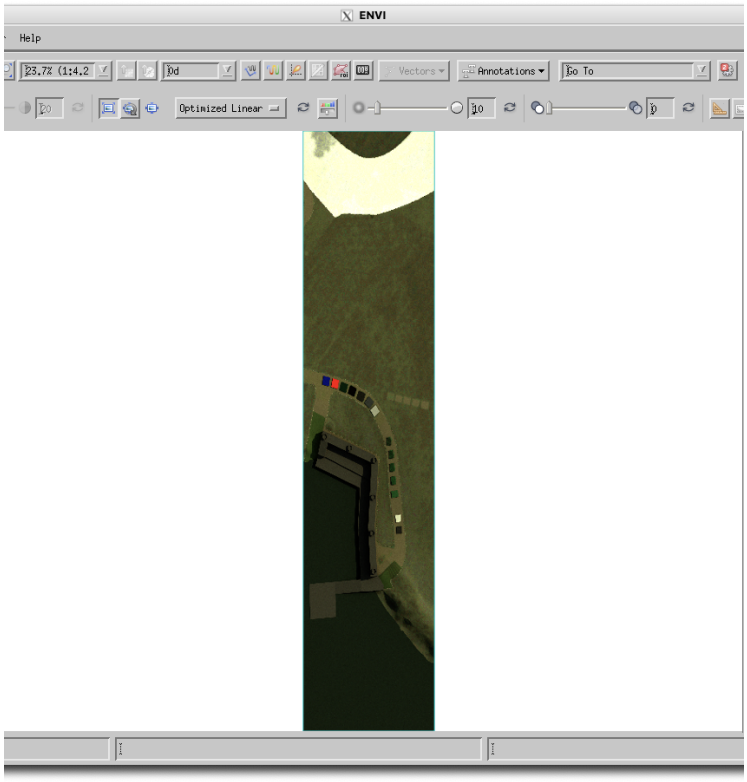

Figure 3.12: Screenshot of the full extent of the DIRSIG-generated base setup in ENVI. Note that the three-dimensional rendering of Tait Preserve is larger than this, but DIRSIG only produces data for what the sensor would have seen given flight and location inputs.

DCs to these other domains for analysis and comparison.

From this point forward, the processing of the DIRSIG data was computed in much the same way as the experimental data. A single truth mask was generated for each of the four DIRSIG-generated scenes (for each of the setups). The reason that only one truth mask was needed for the DIRSIG data compared to the six for the experimental data is because the DIRSIG

data lacked geo-rectification and so a single truth mask could accurately be used for all the setups. Upon generating the truth mask, the mean target radiances for each of the setups was taken as the average of the 100% green target ROI, and the target detection performance analysis was performed in the reflectance domain in the same manner as the experimental data. AUC curves and percent differences were also produced. The results for all of these and an accompanying discussion is given in Section 4.

It was discovered in the processing of the DIRSIG data that the setting of the so-called 'convergence' parameter was essential in producing accurate mean target radiances (and Signal-to-Noise Ratios (SNRs)) for the DIRSIG data. The 'convergence' parameter takes as input three variables: a minimum number of samples per pixel, a maximum number of samples per pixel, and a minimum radiance threshold. DIRSIG uses these variables to determine just how many paths of light it should trace for a given pixel in the scene.

If these variables are not set appropriately, the pixel-to-pixel variability in the resulting DIRSIG data was found to be larger than expected, which impacted the accuracy of the resulting SNRs. It is necessary to ensure that enough samples are being used for every pixel such that the resulting variability in the scene is due to the sensor, and not to the Monte Carlo techniques used to produce the data.

For the mean target radiances and SNRs, the convergence setting was set as $-$**convergence=**100**,**10000**,**$1e-10$, which translated to a minimum

number of samples of 100 and a maximum number samples of $10,000$ per pixel, and a minimum radiance threshold of $10^{-10}\frac{W}{cm^2 sr \mu m}$, which was below the calculated Noise Equivalent Radiance (NER) of the Headwall Nano sensor model used for the DIRSIG and FASSP simulations.

Due to the long computations that were required to attain this high level of convergence, the DIRSIG simulation was limited to only capture the 100% green target panel in the DIRSIG scene using the 'start capture' and 'end capture' parameters. Lines 1752 to 1781 contained the green target panel.

For the target detection performance analysis, the convergence setting was set as $-$**convergence=**60**,**1000**,**$1e-6$, which translated to a minimum number of samples of 60 and a maximum number samples of 1000 per pixel, and a minimum radiance threshold of $10^{-6}\frac{W}{cm^2 sr \mu m}$. This lower convergence setting allowed for quicker computation times, so a larger portion of the scene was captured which contained all of the user-defined ROIs. The 'start capture' and 'end capture' parameters were used to limit the scene between lines 600 and 2120.

3.2.3 FASSP Data Processing

To produce predicted target radiances and target detection performances in FASSP, the reflectance statistics of 14 background classes (shown in Table 3.1) and the 100% green target class from the base setup were utilized. To generate these first- and second- order statistics (mean and covari-

ance), a large number of samples were needed, so the reflectance data from the Headwall Nano was used so several hundred samples for each class could be collected. These statistics were converted into the necessary format for input into FASSP using a Python script written by Chase Cañas. The classes shown in Table 3.1 were chosen to get a good variety of the natural and man-made endmembers present in the data collect so that the most accurate recreation of the experimental collect could be possible.

Table 3.1: Background classes chosen for FASSP runs

Grass	Concrete
Shaded Concrete	Wood Deck
Shaded Wood Deck	Gravel
Red Felt Panel	Light Gray Felt Panel
Gray Felt Panel	Dark Gray Felt Panel
Black Felt Panel	Green Felt Panel
Dark Permaflect Panel	White Permaflect Panel

To ensure a good match with the DIRSIG simulations, the same sensor description was utilized for both DIRSIG and FASSP. This sensor description is shown by the right image in Figure 3.9; it takes as inputs various spectral sensitivities, noise descriptions, bit depth, and sensor dimensions (IFOV/aperture dimensions).

Both the sensor description and the various background and target class descriptions are called by a main script, which contains some important parameters that were edited for each of the setups to get as close of a match up to the DIRSIG simulations and experimental setups. A screenshot of the

Figure 3.13: A screenshot of the main script which was used to run the FASSP simulation for the base setup with its various inputs for the scene, sensor, atmosphere. Not shown here are the inputs for the processing model.

main script which was used to inform the base setup simulation is shown in figure 3.13. The most important parameters utilized for the FASSP runs, as well as their chosen values and descriptions are shown in Table 3.2. The values which change for each setup are in bold.

Using these parameters, FASSP was run for each of the four setups described above and ROC curve results and target radiance spectra were ex-

Table 3.2: Chosen FASSP Parameters for each setup

Variable Name	**Base Setup**	**Shade Setup**	**TR-S Setup**	**TR Setup**	**Description**
metrange	25	25	25	25	meteorological range (km)
solangle	**53.05**	**50.31**	**48.41**	**47.19**	Solar zenith angle (deg)
gndaltitude	0.0	0.0	0.0	0.0	Ground altitude relative to sea level (km)
shadeperc	**0.0**	**100.0**	**100.0**	**0.0**	Percent of target in shade
skyperc	100.0	75.0	50.0	75.0	Percent of sky visible from target
viewangle	5.0	5.0	5.0	5.0	Sensor view angle (degrees, nadir is 0.0)
noisefac	1.0	1.0	1.0	1.0	Sensor noise factor
gainfac	1.0	1.0	1.0	1.0	Gain factor
relcal	0.5	0.5	0.5	0.5	Relative calibration error, %
nbits	12	12	12	12	Number of radiometric bits
platalt	0.064	0.064	0.064	0.064	Sensor altitude (km)
tint	0.009993	0.009993	0.009993	0.009993	Integration time (s)

tracted for comparison to the experimental and DIRSIG results. For the base setup, the *shadeperc* variable was set to 0.0 and the *skyperc* variable was set to 100.0; for the shadowing panel setup, *shadeperc* was set to 100.0 (because the target was completely shadowed) and *skyperc* was set at 75.0; for the TR-S panel setup, *shadeperc* was set at 100.0 and *skyperc* was set to 50.0; and finally, for the TR panel setup, *shadeperc* was set to 0.0 and *skyperc* was set to 75.0 again.

In addition to altering these parameters for each of the setups, the background class percentages and solar angle parameters were altered to align as closely as possible with the experimental conditions. The background class

percentages were set to be equal to the relative size of the ROIs generated with the experimental data. Using these settings, the predicted mean target radiances, SNRs, and ROC Curves were extracted from the FASSP results. These were used, in turn, to produce AUCs and percent differences from the experimental data. They are presented in Chapter 4, along with the DIRSIG and experimental results.

Chapter 4

Results

This Chapter will present the results from each of the aforementioned data sources: experimental results from the Tait Preserve data collect and predicted results from the LMM-based model (FASSP) and the path-tracing model (DIRSIG). Section 4.4 will summarize the performance of the LMM.

4.1 Target Radiance Results

The first result which was analyzed from each of the three data sources was the target radiances, which are shown in Figure 4.1. These four plots show the mean target radiances for the four setups: base setup (top left), shade setup (top right), TR-S setup (bottom left), and TR setup (bottom right). Each plot shows results from the experimental data and the predicted results from DIRSIG and FASSP. All of the plots are shown on the same scale for easy comparison.

From these plots, it is possible to examine how well the LMM-based model (FASSP) and the path-tracing model (DIRSIG) predict the mean radiance of the 100% green target panel for each of the setups. For the base setup,

it is evident that both FASSP and DIRSIG make quite accurate predictions - both match up quite well with the experimental data across all measured wavelengths.

The shadowing (shade) panel setup results show that both DIRSIG and FASSP tend to overestimate the mean target radiance at shorter wavelengths (particularly with the peak at 550 nm, however, DIRSIG seems to more closely align with the experimental results than FASSP, indicating that DIRSIG's

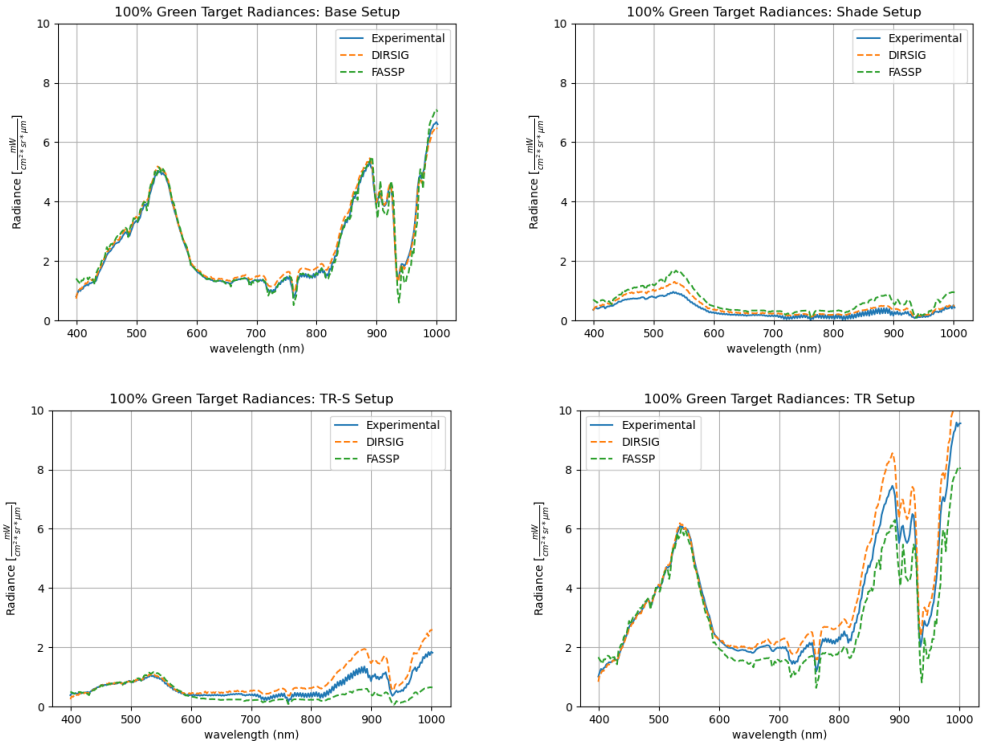

Figure 4.1: The mean target radiances for each of the four setups. Each plot shows the experimental and predicted radiances from DIRSIG and FASSP.

Table 4.1: Target Radiance Percent Differences, %

Modeling Source	**Base Setup**	**Shade Setup**	**TR-S Setup**	**TR Setup**
DIRSIG	3.5	35.1	30.5	9.1
FASSP	0.6	84.7	32.2	14.0

path-tracing technique may account for shadowing better than FASSP.

The results from the TR-S and TR panel setups (bottom row) both show a divergence between the results from DIRSIG and FASSP at wavelengths longer than 600 nm. With each of these plots, it is evident that at longer wavelengths, DIRSIG tends to overestimate mean radiance relative to the experimental results while FASSP tends to underestimate it. Both FASSP's and DIRSIG's predictions align quite well with the experimental results at shorter wavelengths. A close examination of the TR setup results shows that the DIRSIG predictions are slightly more in-line with the experimental results than FASSP's are.

Overall, it is evident from Figure 4.1 that DIRSIG predicts mean target radiances that are more in line with the experimental results whenever non-linear effects (shadowing and adjacent reflections) are present. The percent differences shown in Table 4.1 corroborates this fact. These percent differences were calculated relative to the experimental results and show that in every setup other than the Base Setup, DIRSIG's predictions are closer to the experimental results than FASSP. The difference in accuracy is especially large with the shade setup.

In addition to examining the accuracy of DIRSIG and FASSP relative to the experimental results, the mean target radiances for the 100% green target were also computed for two different types of DIRSIG simulations for the TR-S and TR setups to examine the impact of including the BRF measurement of the TR panel on the resulting target radiances. Figure 4.2 shows the mean target radiances from two DIRSIG simulations and the experimental data.

The first DIRSIG simulation utilized a Lambertian assumption for the TR panel - that is, it assumed that the magnitude of reflected light is independent of the relative location of the sensor. This is in contrast to the second simualtion, which assumed the presence of specular behavior with the TR panel. This simulation utilized the 'ClassicEmissivity' model, which takes as an input a scalar quantity which describes how specular a material is over all wavelengths. A value of 0 indicates Lambertian behavior; a value of 0.9 was used. More information on this plug-in is available in the DIRSIG documentation.

The left plot in Figure 4.2 shows that, when shadowing is present in the DIRSIG scene, a Lambertian TR panel results in a higher mean target radiance at higher wavelengths than a specular TR panel does. In this case, it appears that using a specular TR panel results in more accurate predictions relative to the experimental results than using a Lambertian TR panel does.

The right plot of Figure 4.2 indicates that when shadowing is not present, the specularity of the TR panel does not have any impact on the

resulting mean target radiances of the 100% green target panels. However, these results do show that, overall, the spectrum of TR panel *did* in fact contaminate the mean target spectra of our 100% green target panels - and that incorporating a description of the specularity of the TR panel in the DIRSIG simulations resulted in a better accuracy when shadowing was present.

The mean target radiance results show that

1. Both the LMM-based model (FASSP) and the path-tracing model (DIRSIG) are capable at predicting target radiances when nonlinear effects are *not* present.

2. Both models overestimate the mean target radiance at shorter wavelengths when shadowing is present, however, DIRSIG has better performance than FASSP at all wavelengths.

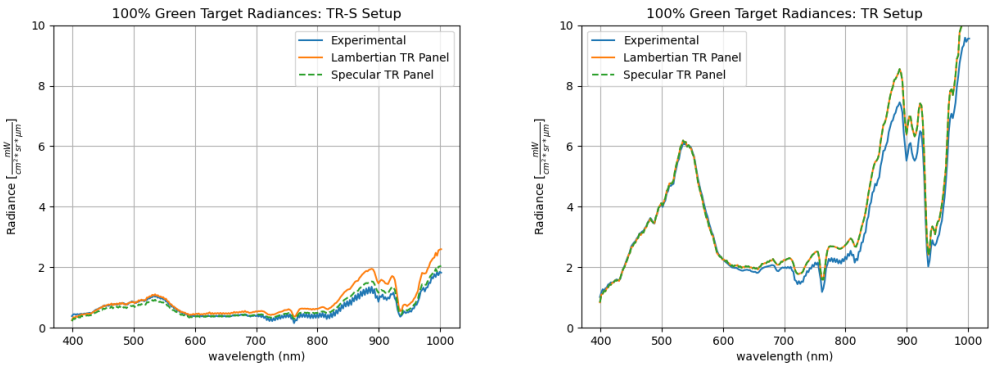

Figure 4.2: The mean target radiances of the 100% green target in the TR-S and TR setups for two DIRSIG simulations with a Lambertian TR panel and Specular TR panel assumption, and also the experimental results.

3. Both FASSP and DIRSIG accurately predict the mean target radiances when the TR and shadowing panels are present at shorter wavelengths; at longer wavelengths, however, DIRSIG overestimates and FASSP underestimates. This is also true when just the TR panel is present.

4. Adjusting the specularity of the TR panel in the DIRSIG simulations impacts the resulting mean target radiances *only* when shadowing is present. A Lambertian TR panel results in higher radiance predictions.

4.2 Signal-to-Noise Ratios

The 100% green target Digital Counts (DCs) were also utilized to produce Signal-to-Noise Ratios (SNRs) for the DIRSIG and Experimental results. FASSP produced the SNRs as a natural output. The SNRs for each of the four setups are shown in Figure 4.3. Each plot shows the SNRs from FASSP, DIRSIG, and the experimental data. For DIRSIG and the experimental results, the SNR was calculated by dividing the mean of the 100% green target ROI by the square root of the variance of the signal of the pixels in this ROI.

In each of the SNR plots, it is evident that, while FASSP produces accurate SNRs relative to the experimental results for both the base and TR setups, DIRSIG accurately predicts the 100% green target SNRs in all circumstances, even when shadowing and adjacent reflections are present. DIRSIG especially outperforms FASSP in the Shade and TR-S setups: an examination of these two plots reveals that FASSP is grossly overestimating the peak sensor

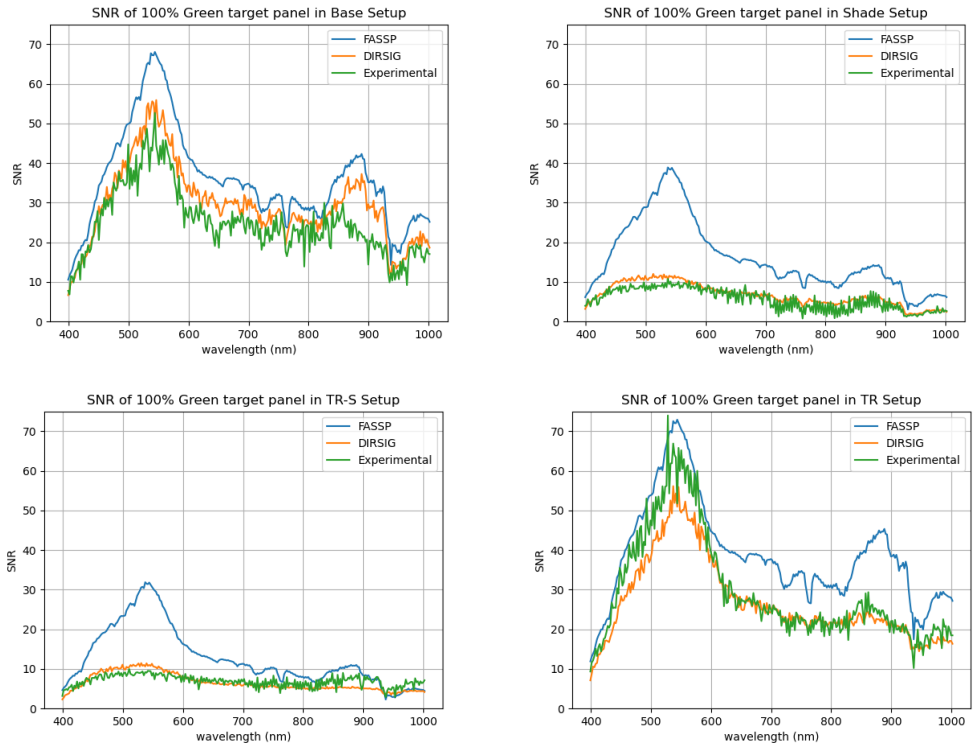

Figure 4.3: The SNRs for each of the four setups of the 100% green target. Each plot shows the results from each of the three data sources.

SNR at 550 nm relative to the experimental results. This matches up with FASSP's mean target radiance predictions in Figure 4.1 for these two setups, where FASSP was predicting much higher radiances relative to the experimental data. In contrast, DIRSIG predicts SNRs that tend to resemble both the shape and magnitude of the experimental results.

4.3 Target Detection Performance Results

This section will review the results from the target detection performance predictions from each of the data sources with the Constrained Energy Minimization (CEM) target detection algorithm. Figure 4.4 shows the detection results from each of the data sources for the base setup.

For each plot shown here (and for the rest in this Section), the probability of detection, P_D, is shown on the vertical axis on a normalized scale and the probability of a false alarm, P_{FA}, is shown on the horizontal axis; it is normalized and on a logarithmic scale. The ROC curve results are plotted for each fill fraction (FF) of sub-pixel target that was placed on the gravel path.

It is important to note that while only the 20% FF line is visible at in the middle of these plots, this is because the rest of the FF targets achieved perfection P_Ds and were found with no false alarms. They are visible - just at the very top of each graph, plotted on top of each other.

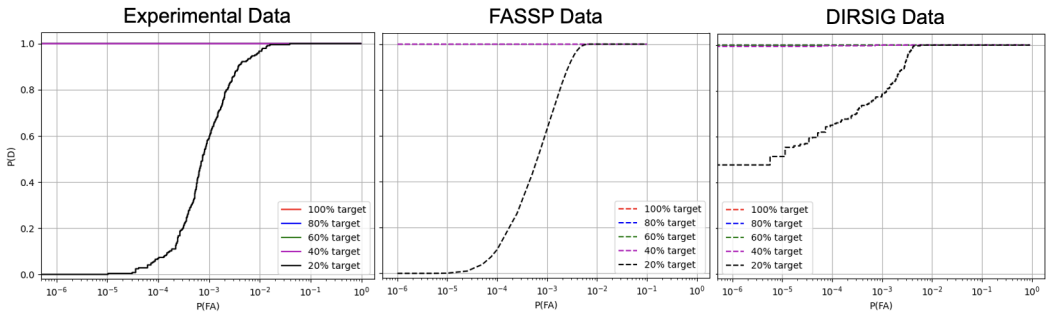

Figure 4.4: Target detection performance from all three data sources for the base setup. Plots include a line for each FF sub-pixel target.

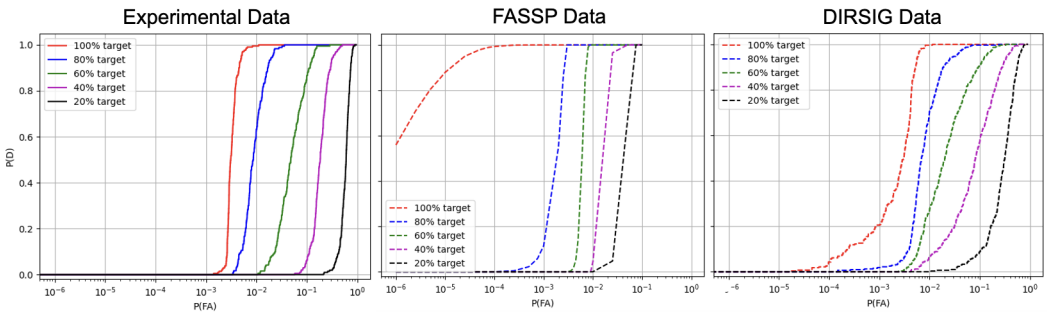

Figure 4.5: Shadowing Panel setup target detection results.

The ROC curves in Figure 4.4 indicate that the LMM-based model (FASSP) is capable of accurately predicting target detection performance when there exists no imposed nonlinear effects in the scene. The fact that the results from DIRSIG do not match up perfectly with the experimental data indicate that it was easier for the sensor and target detection algorithm to find the target pixels than it was in the experimental data or analytical (FASSP) data.

This mismatch could be due to a couple of factors, the most likely of which are that either the DIRSIG data does not contain the correct quantity/quality of noise that is accurate to either the experimental or analytical data or it could be due to user-defined truth mask. The data from the experimental and DIRSIG data require subjective input to indicate where the target and background pixels are present in an image - a slightly more conservative selection with DIRSIG could arbitrarily increase its performance.

Figure 4.5 depicts the target detection predictions with the shadowing panel setup. Through comparison with the experimental data, it is evident

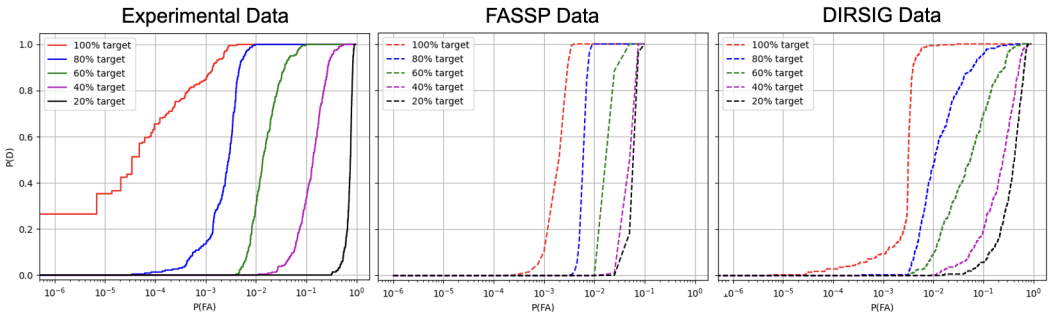

Figure 4.6: TR-S panel setup target detection results.

that FASSP appears to overestimate detection performance for every FF target in the shadowing panel setup. While DIRSIG still delivers overestimates, its predictions are better across the board and better resemble the shape of the experimental ROC curves.

When considering the target radiance predictions for the shadowing setup shown in Figure 4.1, this is not all that surprising - FASSP consistently predicts a higher target radiance than DIRSIG and the experimental results across all wavelengths. This higher target radiance would indicate that FASSP is predicting a higher signal from the target than is actually present, which would make it easier to be detected.

Figure 4.6 depicts the detection performance for the TR-S panel setup. From these plots, it is apparent that, with the exception of the 20% FF target DIRSIG's detection performance predictions align quite well with that of the experimental data. This is in contrast to FASSP's predictions, which appear to align well for the 80% and 60% FF targets, but not as well for the 40% and 20%

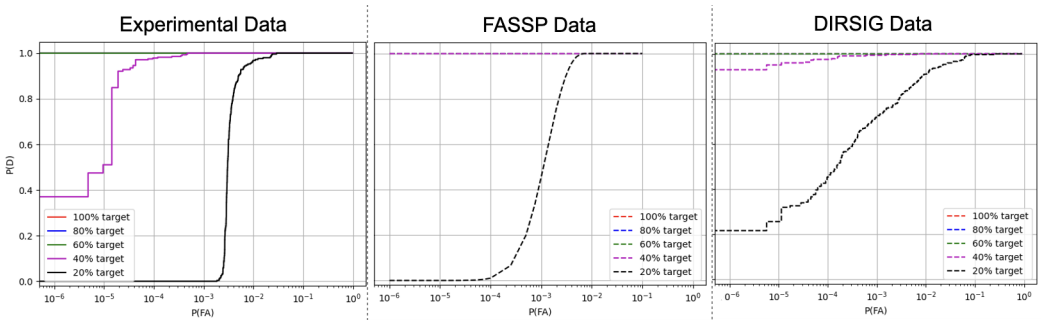

Figure 4.7: TR panel setup target detection results.

targets. DIRSIG's accuracy with its detection performance predictions with both the shadowing and TR panels present indicate that it is able to replicate both nonlinear effects quite accurately in its synthetic data generation process.

Figure 4.7 shows the target detection performance in the TR panel setup. From these plots, it is apparent that, with respect to the experimental data, FASSP predicts the 20% target performance more accurately than DIRSIG, but DIRSIG is able to accurately predict the existence of several false alarms with the 40% target that cause it to have an imperfect P_D. This is in contrast to the FASSP results, which predict perfect detection for the higher FF targets.

Figure 4.8 shows the Area-Under-the-Curves (AUCs) for the three data sources. The AUC is calculated by summing up the total normalized area under the ROCs in the corresponding setup for the corresponding Fill Fraction (FF) target. An AUC of 1.00 indicates perfect detection and no false alarms for that FF target.

The vertical axis on each plot is limited between 0.70 and 1.00 to highlight the differences in magnitude between the different setups. For this reason, the results in the Base and TR setups appear as lines at the very top of the plot - the AUCs for all of the FF targets in these setups are very nearly equal to 1.00. This is in contrast to the Shade and TR-S setups, where it is evident that the AUCs drop-off quickly for the lower FF targets. The results in the Shade and TR-S plots also show that, in both setups, DIRSIG predicts the drop-off more accurately than FASSP does. The AUCs further emphasize the conclusion that when shadowing is present, DIRSIG is able to more accurately account for its impact on a target detection task than FASSP is.

Table 4.2 shows the percent differences between the DIRSIG and FASSP AUCs and the experimental AUCs. This table shows the percent differences for each Fill Fraction (FF) target in each of the four setups. The DIRSIG percent differences are shown in **boldface**. Together, the AUCS and AUC percent differences highlight that both DIRSIG and FASSP both predict similar performances to the experimental results in the Base and TR

Table 4.2: ROC Curve Percent Differences, **DIRSIG**/FASSP, %

Target Fill Fraction	**Base Setup**	**Shade Setup**	**TR-S Setup**	**TR Setup**
100%	**0.0**/0.1	**0.0**/4.2	**0.3**/5.8	**0.0**/0.1
80%	**0.0**/0.0	**0.2**/0.7	**2.4**/4.7	**0.0**/0.0
60%	**0.0**/0.0	**2.3**/6.0	**8.1**/0.0	**0.0**/0.0
40%	**0.0**/0.0	**9.3**/25.7	**16.1**/18.5	**0.0**/0.0
20%	**0.1**/0.2	**68.6**/162.4	**134.1**/321.0	**0.1**/0.4

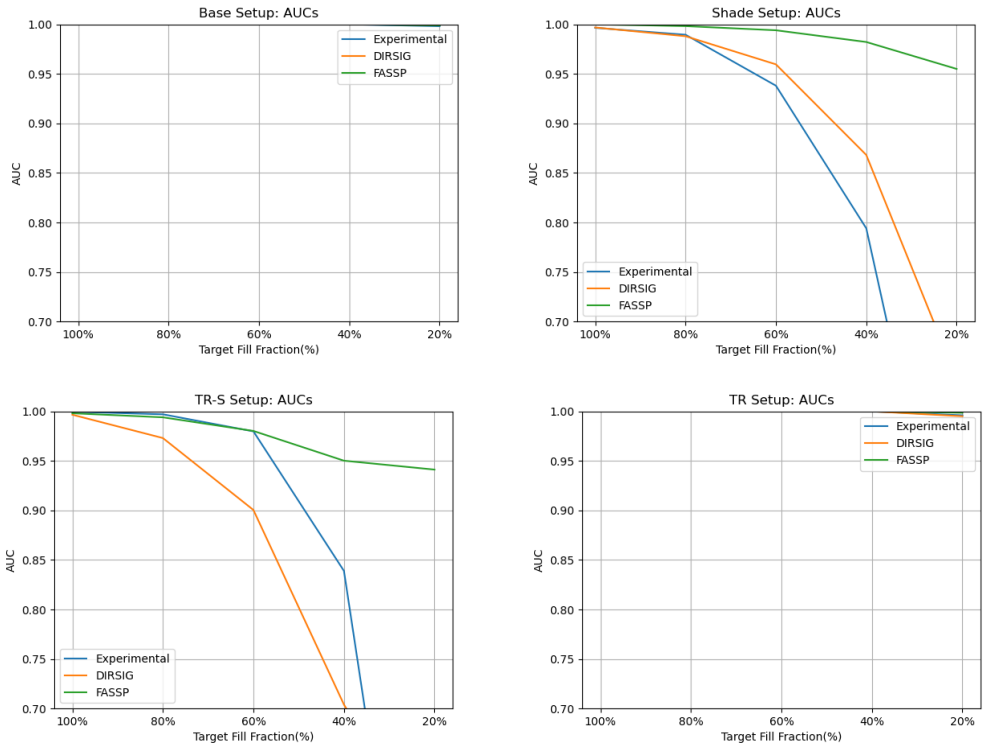

Figure 4.8: Area-Under-the-Curves (AUCs) plotted for each of the data sources in all four setups. Note that the vertical axis on each plot is limited between 0.70 and 1.00 for an easier comparison of the magnitude of difference between the setups.

setups, but in the Shade and TR-S setups, DIRSIG performs quite a bit better than FASSP does. In both of these setups, this gap in performance is quite large, especially with the 20% FF target, where DIRSIG is more than twice as accurate than FASSP. These percent differences were calculated using $Error_{\%} = \frac{prediction - experimental}{experimental} * 100\%$ for each of the AUC data points in each of the four setups.

From these results, it is possible to make the following conclusions:

1. As they are currently configured, both models (FASSP and DIRSIG) perform similarly when no nonlinear effects are present (base setup).

2. The impact of the TR panel does not result in significant predictive performance differences for either DIRSIG or FASSP when the target is *not* in shadow. This is evident by minuscule changes in percent differences in the Base and TR setups found in Table 4.2 and the AUCs in Figure 4.8.

3. The LMM-based model (FASSP) is able to accurately predict target detection performances when the target is not in shadow. When the shadow is in target, the path-tracing model (DIRSIG) is essential to ensure better predictive performance. The large percent differences in Table 4.2 and the performance predictions evident in the AUCs in Figure 4.8 corroborate this.

4.4 Linear Mixing Model Performance

Given the results in the above sections, it is hopefully more apparent what environmental conditions are necessary to cause a significant reduction in accuracy of any LMM-leveraged model, such as FASSP.

With the predicted mean target radiances, the LMM (FASSP) is able to produce more accurate results when shadowing is *not* present (the Base and

TR setups). However, the presence of the TR panel (adjacent reflections) and the inability of FASSP to utilize any description of this effect in its simulations, did result in a higher error with the TR setup than was present with just the Base setup. An examination of Figure 4.1 and Table 4.1 both show this.

On the other hand, DIRSIG appears to more accurately consider the impact of shadowing (shade panel) and adjacent reflections (TR panel) in its simulations. It is the belief of this thesis that the accuracy of DIRSIG's results could further be improved upon to reduce the errors present in the mean target radiances and SNRs.

The SNRs (Figure 4.3) show a significant difference between the empirical and FASSP results when shadowing is present. It appears that some of the error in FASSP's SNR predictions are due to its mean target radiance predictions in Figure 4.1; the higher-than-realistic predicted signal from FASSP in the shadowing and TR-S setups would contribute to a higher SNR than is being seen with the empirical data. In contrast, DIRSIG appears to be better considering the impact of shadowing. Both FASSP and DIRSIG appear to consider the impact of adjacent reflections (the TR setup) in their SNR calculations.

As there are so many data points present in the ROC curves and as they are plotted on a logarithmic horizontal scale, the overall performance of the target detection performances is probably best assessed using Table 4.2 and Figure 4.8. Table 4.2 indicates that the performance of both DIRSIG and

FASSP with higher FF targets (100%, 80%, and 60%) are on the same scale.

With the lower FF targets (40% and 20%), however, higher error is seen with the LMM-based model (FASSP) than with the path-tracing model regardless of the setup. As seen with the mean target radiances and SNRs, shadowing has the most detrimental impact on the accuracy of the LMM (and also DIRSIG). Adjacent reflections (the TR panel), appear to have an almost-negligible impact. With both, DIRSIG appears to better consider these effects. The AUCs in Figure 4.8 corroborate these statements.

Chapter 5

Summary

Since its advent in the early 1980s, Hyperspectral Imaging (HSI) sensors have collected high-resolution spectral information of the Earth's surface. Despite many design improvements in the approximately 3 decades since, challenges in using HSI sensors to detect sub-pixel sized targets in cluttered backgrounds still exist. To address these difficulties, much work has been accomplished, specifically to develop better theoretical models which more accurately describe HSI data, to develop modeling software which can produce accurate system analyses, and to collect high fidelity HSI data to inform research efforts.

The Linear Mixing Model (LMM) is a HSI data model that proposes that the interaction between light and materials in a scene occurs in a linear manner, and as such, the signal detected by a given HSI pixel can be expressed as the linear combination of the pure materials present in the pixel's projected area on the ground weighted by their relative abundances. As a result of the general veracity of its claims, the LMM is a well-established and relied upon basis within the regime of HSI target detection. However, when nonlinear effects, such as shadowing and multiple reflections, are present, LMM-based methods tend to break down.

The primary objective of this thesis is to investigate the impact of nonlinear effects on HSI target sub-pixel target detection. To this end, an experimental data collect with a novel experimental design that imposed controlled nonlinear effects was conducted in September 2022 at Rochester Institute of Technology's (RIT) Tait Preserve in Rochester, New York. The results of this experimental collect were compared with those from two types of modeling software: the Forecasting and Analysis of Spectroradiometric System Performance (FASSP) model [23, 24] and the Digital Imaging and Remote Sensing Image Generation (DIRSIG) model [11].

FASSP's computations are founded on the basis of the LMM, and as such, its results are representative of what the LMM model would predict given numerous parameters describing a scene setup, atmospheric conditions, and a sensor. In contrast, the DIRSIG model utilizes a path-tracing model which is able to capture the impact of nonlinear effects which are present here. To inform its computations, DIRSIG includes in its inputs a 3-dimensional scene geometry, material properties, a description of a sensor and its motion relative to the scene, and material specularity.

Work was then conducted to produce comparable results from each of these data sources for comparison, which would allow for an inspection of LMM performance when nonlinear effects are present. Two main types of data were produced using this methodology: mean target radiances (and by extension, Signal-to-Noise Ratios (SNRs)) and target detection performances

in the form of Receiver Operating Characteristic (ROC) Curves and Area-Under-the-Curves (AUCs).

From the results, the following conclusions could be made:

1. Both the LMM-based model (FASSP) and the path-tracing model are capable at predicting mean target radiances/SNRs when nonlinear effects are *not* present. The impact of shadowing is significantly more detrimental to the accuracy of these models than adjacent reflections are.

2. The path-tracing paradigm of DIRSIG is better able to consider the impact of both shadowing and adjacent reflections in its simulations. However, it should be noted that careful attention should be given to the 'convergence' setting within DIRSIG.

3. In the prediction of target detection performance (ROC Curves and AUCs) the impact of shadowing was found to be substantially more detrimental to the performance of the LMM-based model than adjacent reflections were. DIRSIG appears to better consider both of these effects.

In the context of our experimental collect and subsequent modeling, the LMM appears to suffer most dramatically when shadowing is present. The adjacent reflections which were imposed in our data, both empirically and in our modeling, appear to certainly result in some differences in the

mean target radiances, and target detection performance, but to a degree that could be described as minor when compared to the impact of shadowing. This is not necessarily true for all circumstances containing adjacent reflections.

These results indicate the need for future work to continue to investigate the performance of FASSP and DIRSIG with respect to the experimental data. The results from DIRSIG, specifically, have undergone many iterations to determine the proper input parameters; more work in this regard would be helpful to determine exactly where its modeling limitations are.

Chapter 6

Future Work

The work which was conducted for this thesis was certainly a good step to investigate the impact of some controlled nonlinear effects on the performance of the Linear Mixing Model (LMM). However, the modeling software which was used for this research (FASSP and DIRSIG), both contain numerous user inputs for scene, atmosphere, sensor, and post-processing descriptions, and as such, there exists many seemingly-minor changes that could be made to improve the final results. Some avenues of future work include:

1. Improve understanding and performances of both FASSP and DIRSIG both when nonlinear effects are and are not present. This work has identified shadowing of a target to be largely responsible for the breakdown of the LMM relative to a path-tracing model (DIRSIG), however, further work could be aimed to better quantify this breakdown.

2. Better characterize the role that atmospheric conditions play in DIRSIG simulations when nonlinear effects are present. It was found that adjusting the atmospheric parameters resulted in substantial impacts on the resulting data.

3. Improve the implementation of FASSP such that it better considers non-linear effects in its computations. Such improvements could include descriptions for adjacent objects' spectral contamination of a target.

4. Improve the Tait Preserve scene that has been generated for DIRSIG simulation purposes. The current scene that exists and the newly-implemented FASSP sensor plug-in could be responsible for much of the error present in the DIRSIG predictions relative to the empirical results.

5. Apply Dr. Ientilucci's LIDAR-informed atmospheric compensation method [18] to optimize target detection performance in the setups where the shadowing and TR panels are present.

Appendix

The following tables provide additional information about the data processing for the Experimental, FASSP, and DIRSIG data.

Table A1 shows some relevant information pertaining to the experimental data collect conducted at Tait Preserve on September 9, 2022. With access to the Rochester Institute of Technology (RIT) Chester F. Carlson Center for Imaging Science (CIS)'s Linux database of collected Unmanned Aircraft System (UAS) data, the mission and flight numbers could be used to extract the Digital Count (DC), radiance, and reflectance data that was used within the data processing used for this thesis.

Table A2 shows the pixel counts for the target ROIs (100%, 80%, 60%, 40%, and 20%) FF targets) for each of the four setups for the **experimental** and DIRSIG data. Note that the experimental ROI pixel counts (and also the resulting background class percentages) are what was used to inform the FASSP simulations.

Table A1: Headwall Nano information used for experimental data analysis

Setup Type	Mission Number	Flight Number	Time of Flight (ET)	Solar Zenith Angle
Base	1453	4432	10:50	50.048°
Shadowing	1515	4528	11:15	53.310°
TR-S	1537	4528	11:35	48.414°
TR	1557	4544	11:50	47.187°

Table A2: **Experimental**/DIRSIG data target ROI pixel counts. Note that the FASSP pixel counts are equal to the experimental ones.

Target ROIs	**100**% FF	**80**% FF	**60**% FF	**40**% FF	**20**% FF
Base Setup	**337**/278	**294**/320	**285**/304	**269**/327	**245**/300
Shadowing Setup	**211**/278	**180**/320	**194**/304	**202**/327	**211**/300
TR-S Setup	**238**/278	**231**/320	**222**/304	**239**/327	**224**/300
TR Setup	**309**/278	**270**/320	**286**/304	**278**/327	**252**/300

Table A3 shows the pixel counts for every background class used in the experimental and DIRSIG data analyses for each of the target setups. Note

Table A3: **Experimental**/DIRSIG data background ROI pixel counts. Note that the FASSP pixel counts are equal to the experimental ones.

ROIs	Base Setup	Shadowing Setup	TR-S Setup	TR Setup
Grass	**3,183,184**/ 796,622	**3,124,629**/ 796,622	**3,161,658**/ 796,622	**3,133,202**/ 796,622
Concrete	**169,356**/ 137,339	**125,291**/ 137,339	**127,466**/ 137,339	**187,430**/ 137,339
Shaded Concrete	**5,416**/11,577	**4,119**/11,577	**4,195**/11,577	**5,703**/11,577
Wood Deck	**1,442**/	**846**/	**464**/	**581**/
Shaded Wood Deck	**1,387**/	**997**/	**577**/	**715**/
Gravel	**3,269**/2,043	**2,632**/2,043	**1,265**/2,043	**1,186**/2,043
White Permaflect	**2,754**/5,886	**1,549**/5,886	**1,822**/5,886	**1,834**/5,886
Dark Permaflect	**420**/ 391	**248**/ 391	**322**/ 391	**381**/ 391
Red Felt	**306**/ 320	**267**/ 320	**180**/ 320	**277**/ 320
Green Felt	**636**/ 500	**422**/ 500	**159**/ 500	**464**/ 500
Black Felt	**495**/ 517	**390**/ 517	**453**/ 517	**518**/ 517
Dark Gray Felt	**427**/ 501	**354**/ 501	**482**/ 501	**499**/ 501
Light Gray Felt	**486**/ 539	**378**/ 539	**436**/ 539	**429**/ 539
White Felt	**434**/ 529	**376**/ 529	**465**/ 529	**426**/ 529
Guard Region	**425**/ 552	**317**/ 552	**486**/ 552	**428**/ 552

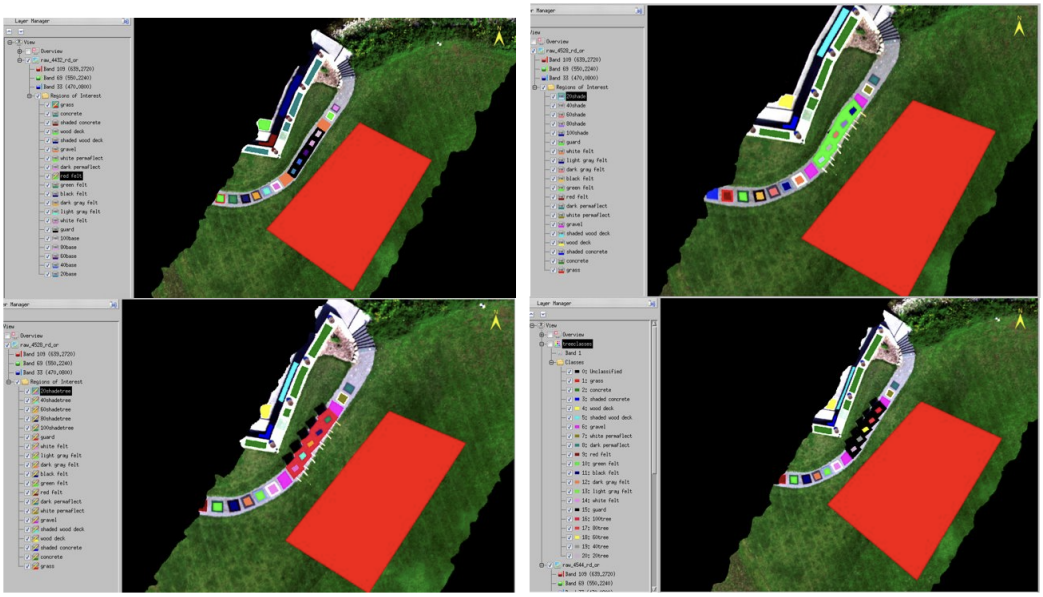

Figure A1: Screenshots in ENVI of the user-defined truth masks used for the experimental data processing. Top left image is the base setup, top right is the shadowing setup, bottom left is the TR-S setup, and bottom right is the TR setup.

that the FASSP pixel counts for these background classes are equal to the experimental ones. It is also important to note that while there were ROIs generated for the 'Wood Deck' and 'Shaded Wood Deck' classes in the experimental data, these classes were not present in the DIRSIG Tait Preserve scene. Instead those, regions of the Tait Preserve scene belonged to the 'Concrete' and 'Shaded Concrete' ROIs, so those pixels, although named as belonging to the 'Wood Deck' and 'Shaded Wood Deck' ROIs, instead counted towards the 'Concrete' and 'Shaded Concrete' ROIs.

Figure A1 shows screenshots of the user-defined truth masks that were

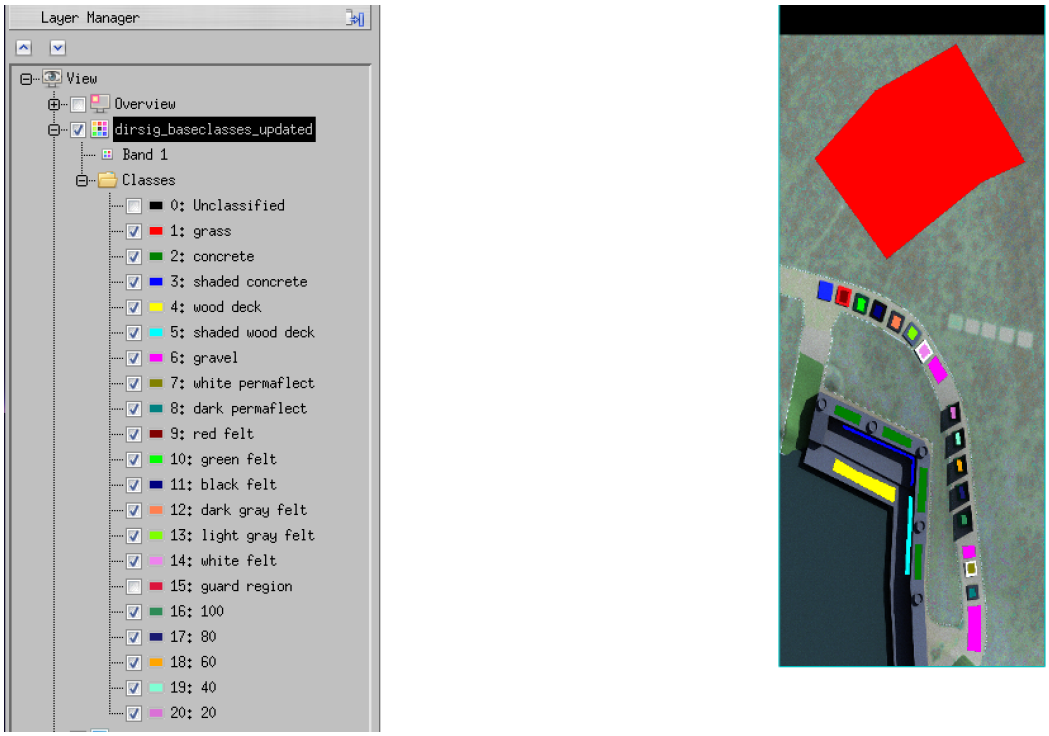

Figure A2: Screenshot in ENVI showing the DIRSIG truth mask. This truth mask was used for all of the setups, as the DIRSIG data was not georectified.

used for the experimental data processing for each of the four setups. There were 20 classes generated in total: 5 target classes, 1 guard region to prevent unnecessary false alarms, and 14 background classes.

Figure A2 shows a screenshot in ENVI of the truth mask which was defined and used with the DIRSIG data. As the DIRSIG data is not georectified, this truth mask was used for all of the setups (base, shadowing, TR-S, and TR). In addition, as noted above, although they are named as such, the 'Wood Deck' and 'Shaded Wood Deck' ROIs are instead a part of the 'Con-

crete' and 'Shaded Concrete' classes. This is because the wood deck next to the lake at Tait Preserve was not represented in the Tait scene, instead, it was treated as more concrete. This fact means that while there existed 14 background classes for the experimental data analysis, there only existed 12 for the DIRSIG analysis.

Bibliography

[1] A. Berk and et. al. MODTRAN6: a major upgrade of the MODTRAN radiative transfer code. volume 9088, page 90880H. SPIE, SPIE, 2014.

[2] José M. Bioucas-Dias, Antonio Plaza, Nicolas Dobigeon, Mario Parente, Qian Du, Paul Gader, and Jocelyn Chanussot. Hyperspectral unmixing overview: Geometrical, statistical, and sparse regression-based approaches. *IEEE Journal of Selected Topics in Applied Earth Observations and Remote Sensing*, 5(2):354–379, 2012.

[3] Scott Brown, J. Schott, and R. Raqueno. Evaluation of dirsig for solar and emissive region hyperspectral image simulations. In *Proceedings of the Ground Target Modeling and Validation Conference*, 1998.

[4] Scott Brown, J. Schott, R. Raqueno, T. Kraska, and R. White. Validation and analysis of the digital imaging and remote sensing laboratory's synthetic image generation model, dirsig. In *Proceedings of the Ground Target Modeling and Validation Conference*, 1996.

[5] Scott D. Brown, Daniel D. Blevins, and John R. Schott. Time-gated topographic LIDAR scene simulation. In Gary W. Kamerman, editor, *Laser Radar Technology and Applications X*, volume 5791, pages 342 – 353. International Society for Optics and Photonics, SPIE, 2005.

[6] Chase Cañas, John P Kerekes, Emmett J Ientilucci, and Scott D Brown. Empirical validation of a hyperspectral systems model for subpixel target detection using data from a new UAS field collection. In Emmett J Ientilucci and Christine L Bradley, editors, *Imaging Spectrometry XXV: Applications, Sensors, and Processing*, volume 12235, page 122350E. International Society for Optics and Photonics, SPIE, 2022.

[7] Chase Cañas, John P Kerekes, Colin Maloney, Emmett J Ientilucci, and Scott D Brown. Impacts of Fully Illuminated Targets On Partially Shaded Backgrounds for a Multiclass Subpixel Target Detection Scenario. pages 2266–2269. International Geoscience and Remote Sensing Symposium, IGARSS, 2023.

[8] M. Eismann. *Hyperspectral Remote Sensing*. SPIE Press, Bellingham, Washington, 2012.

[9] AnneMarie Giannandrea, Nina Raqueno, David W Messinger, Jason Faulring, John P Kerekes, Jan van Aardt, Kelly Canham, Shea Hagstrom, Erin Ontiveros, Aaron Gerace, Jason Kaufman, Karmon M Vongsy, Heather Griffith, Brent D Bartlett, Emmett Ientilucci, Joseph Meola, Lauwrence Scarff, and Brian Daniel. The SHARE 2012 data campaign. In Sylvia S Shen and Paul E Lewis, editors, *Algorithms and Technologies for Multispectral, Hyperspectral, and Ultraspectral Imagery XIX*, volume 8743, page 87430F. International Society for Optics and Photonics, SPIE, 2013.

[10] Alexander F H Goetz, Gregg Vane, Jerry E Solomon, and Barrett N Rock. Imaging Spectrometry for Earth Remote Sensing. *Science*, 228(4704):1147–1153, 1985.

[11] A. Goodenough and S. Brown. Dirsig5: Next-generation remote sensing data and image simulation framework. *IEEE JSTARS*, 10:4818–4833, 11 2017.

[12] R.O. Green and et. al. Imaging spectroscopy and the airborne visible/infrared imaging spectrometer (aviris). *RSE*, 65(3):227–248, 1998.

[13] John A. Hackwell, David W. Warren, Robert P. Bongiovi, Steven J. Hansel, Thomas L. Hayhurst, Dan J. Mabry, Mazaher G. Sivjee, and James W. Skinner. Lwir/mwir imaging hyperspectral sensor for airborne and ground-based remote sensing. In *Optics & Photonics*, 1996.

[14] J. Harms. *The Design and Implementation of GRIT-T: RIT's Next-generation Field Portable Goniometer System*. PhD thesis, Rochester Institute of Technology, 2016.

[15] Jared Herweg, John P. Kerekes, Oliver Weatherbee, David W. Messinger, Jan A. N. van Aardt, Emmett Ientilucci, Zoran Ninkov, Jason W. Faulring, Nina G. Raqueno, and Joseph Meola. Spectir hyperspectral airborne rochester experiment data collection campaign. In *Defense + Commercial Sensing*, 2012.

[16] Emmett Ientilucci. SHARE 2012: Analysis of Illumination Differences on Targets in Hyperspectral Imagery. volume 8743, 2013.

[17] Emmett Ientilucci. Target detection assessment of the SHARE 2010/2012 hyperspectral data collection campaign. volume 9472, 2015.

[18] Emmett J. Ientilucci. Leveraging lidar data to aid in hyperspectral image target detection in the radiance domain. In Sylvia S. Shen and Paul E. Lewis, editors, *Algorithms and Technologies for Multispectral, Hyperspectral, and Ultraspectral Imagery XVIII*, volume 8390, page 839007. International Society for Optics and Photonics, SPIE, 2012.

[19] Emmett J. Ientilucci and Steven Adler-Golden. Atmospheric compensation of hyperspectral data: An overview and review of in-scene and physics-based approaches. *IEEE Geoscience and Remote Sensing Magazine*, 7(2):31–50, 2019.

[20] Emmett J. Ientilucci, Scott D. Brown, John R. Schott, and Rolando V. Raqueno. Multispectral simulation environment for modeling low-light-level sensor systems. In *Image Intensifiers and Applications; and Characteristics and Consequences of Space Debris and Near-Earth Objects*, volume 3434 of *Society of Photo-Optical Instrumentation Engineers (SPIE) Conference Series*, pages 10–19, November 1998.

[21] Emmett J. Ientilucci and Michael Gartley. Impact of BRDF on physics-based modeling as applied to target detection in hyperspectral imagery.

In Sylvia S. Shen and Paul E. Lewis, editors, *Algorithms and Technologies for Multispectral, Hyperspectral, and Ultraspectral Imagery XV*, volume 7334 of *Society of Photo-Optical Instrumentation Engineers (SPIE) Conference Series*, page 73340T, May 2009.

[22] Digital Imaging and Remote Sensing Laboratory. Dirsig model introduction, 2023.

[23] J.P. Kerekes and J.E. Baum. Spectral Imaging System Analytical Model for Subpixel Object Detection. *IEEE TGRS*, 40(5):1088–1101, 2002.

[24] J.P. Kerekes and J.E. Baum. Full Spectrum Spectral Imaging System Analytical Model. *IEEE TGRS*, 43(3):571–580, 2005.

[25] Klaus Mangold, Joseph Shaw, and Michael Vollmer. The physics of near-infrared photography. *European Journal of Physics*, 34:51–, 11 2013.

[26] D. Manolakis and G. Shaw. Detection algorithms for hyperspectral imaging applications. *IEEE Signal Processing Magazine*, 19(1):29–43, 2002.

[27] D. Manolakis, C. Siracusa, and G. Shaw. Hyperspectral subpixel target detection using the linear mixing model. *IEEE TGRS*, 39(7):1392–1409, 2001.

[28] John E. Mason, John R. Schott, and Donna Rankin-Parobek. Validation analysis of the thermal and radiometric integrity of RIT's synthetic image generation model, DIRSIG. In Wendell R. Watkins and Dieter

Clement, editors, *Characterization and Propagation of Sources and Backgrounds*, volume 2223 of *Society of Photo-Optical Instrumentation Engineers (SPIE) Conference Series*, pages 474–487, June 1994.

[29] F. E. et. al. Nicodemus. Considerations and nomenclature for reflectance, 1977.

[30] Headwall Photonics. Headwall photonics. `https://www.headwallphotonics.com`, 2022.

[31] Hsuan Ren, Qian Du, Chein-I Chang, and J O Jensen. Comparison between constrained energy minimization based approaches for hyperspectral imagery. pages 244–248, 2003.

[32] Lee J. Rickard, Robert W. Basedow, Edward F. Zalewski, Peter R. Silverglate, and Mark Landers. HYDICE: an airborne system for hyperspectral imaging. In Gregg Vane, editor, *Imaging Spectrometry of the Terrestrial Environment*, volume 1937, pages 173 – 179. International Society for Optics and Photonics, SPIE, 1993.

[33] J. Salacain, Scott Brown, R. Raqueno, and J. Schott. Incorporation of sensor geometry effects in synthetic image generation models. In *Proceedings of the Ground Target Modeling and Validation Conference*, pages 420–434, 1995.

[34] Neil W. Scanlan, John R. Schott, and Scott D. Brown. Performance analysis of improved methodology for incorporation of spatial/spectral variability in synthetic hyperspectral imagery. In *Imaging Spectrometry IX*, volume 5159 of *Society of Photo-Optical Instrumentation Engineers (SPIE) Conference Series*, pages 319–330, January 2004.

[35] SEOS. Introduction to categorisation of objects from their data, 2023.

[36] James Shell and John Schott. A polarized clutter measurement technique based on the governing equation for polarimetric remote sensing in the visible to near infrared. In *Targets and Background XI: Characterization and Representation*, volume 5811. International Society for Optics and Photonics, SPIE, 2005.

[37] Robert Singer and Thomas McCord. Mars - Large scale mixing of bright and dark surface materials and implications for analysis of spectral reflectance. In *Lunar and Planetary Science Conference Proceedings*, volume 2, pages 1835–1848. Pergamon Press, Inc., 1979.

[38] Ben Somers, Maciel Zortea, Antonio Plaza, and Gregory Asner. Automated extraction of image-based endmember bundles for improved spectral unmixing. *IEEE Journal of Selected Topics in Applied Earth Observations and Remote Sensing - IEEE J SEL TOP APPL EARTH OBS*, 5:396–408, 04 2012.

[39] G. Vaughan and W. Calvin. Mapping weathering and alteration minerals in the comstock and geiger grade areas using visible to thermal infrared airborne remote sensing data. 2005.

[40] Sandra Wiseman, Steve Adler-Golden, Emmett Ientilucci, and Timothy Perkins. Enhanced target detection under poorly illuminated conditions. In *2021 IEEE International Geoscience and Remote Sensing Symposium IGARSS*, pages 1425–1428, 2021.

[41] Naoto Yokoya, Norihide Miyamura, and Akira Iwasaki. Preprocessing of hyperspectral imagery with consideration of smile and keystone properties. In Allen M Larar, Hyo-Sang Chung, and Makoto Suzuki, editors, *Multispectral, Hyperspectral, and Ultraspectral Remote Sensing Technology, Techniques, and Applications III*, volume 7857, page 78570B. International Society for Optics and Photonics, SPIE, 2010.

[42] R. Zhao and E. Ientilucci. A full-spectrum spectral imaging system analytical model with lwir tes capability. *IEE TGRS*, 60(5534409):1–9, 2022.

Index